Disentangling the sequence, cellular and ultrastructural determinants of Huntingtin nuclear and cytoplasmic inclusion formation.

Nathan Riguet[1], Anne-Laure Mahul-Mellier[1], Niran Maharjan[1], Johannes Burtscher[1], Alice Patin[1], Marie Croisier[2], Graham Knott[2], Veronika Reiterer[3], Hesso Farhan[3] and Hilal A. Lashuel[1]*

*Correspondence: hilal.lashuel@epfl.ch

Affiliations:

[1]Laboratory of Molecular and Chemical Biology of Neurodegeneration, Brain Mind Institute, Ecole Polytechnique Fédérale de Lausanne (EPFL), 1015 Lausanne, Switzerland.

[2]BIO EM facility (BIOEM), EPFL, 1015 Lausanne, Switzerland.

[3]Institute of Basic Medical Sciences, University of Oslo, Norway.

Running title:

Ultrastructure and composition of cellular Huntingtin inclusions

Keywords:

Huntington's Disease, Huntingtin, Httex1, Inclusion, Polyglutamine, Nt17, GFP, Fibrils, Electron Microscopy, 3D modeling, CLEM, Proteomics

Abstract

Despite the strong evidence linking the aggregation of the Huntingtin protein (Htt) to the pathogenesis of Huntington's disease (HD), the mechanisms underlying Htt aggregation and neurodegeneration remain poorly understood. Herein, we investigated the ultrastructural properties and protein composition of Htt inclusions in cells overexpressing mutant exon1 of the Htt protein. Our findings provide novel insight into the ultrastructural properties of cytoplasmic and nuclear Htt inclusions and their mechanisms of formation. We show that Htt inclusion formation and maturation are complex processes that, although initially driven by polyQ-dependent Htt aggregation, also involve 1) polyQ and PRD domain-dependent sequestration of lipids and cytoplasmic and cytoskeletal proteins related to HD dysregulated pathways; 2) recruitment and accumulation of remodeled or dysfunctional membranous organelles; and 3) impairement of the protein quality control and degradation machineries. Interestingly, nuclear and cytoplasmic Htt inclusions exhibited distinct biochemical composition and ultrastructural properties, suggesting different formation mechanisms and toxicity.

Graphical Abstract

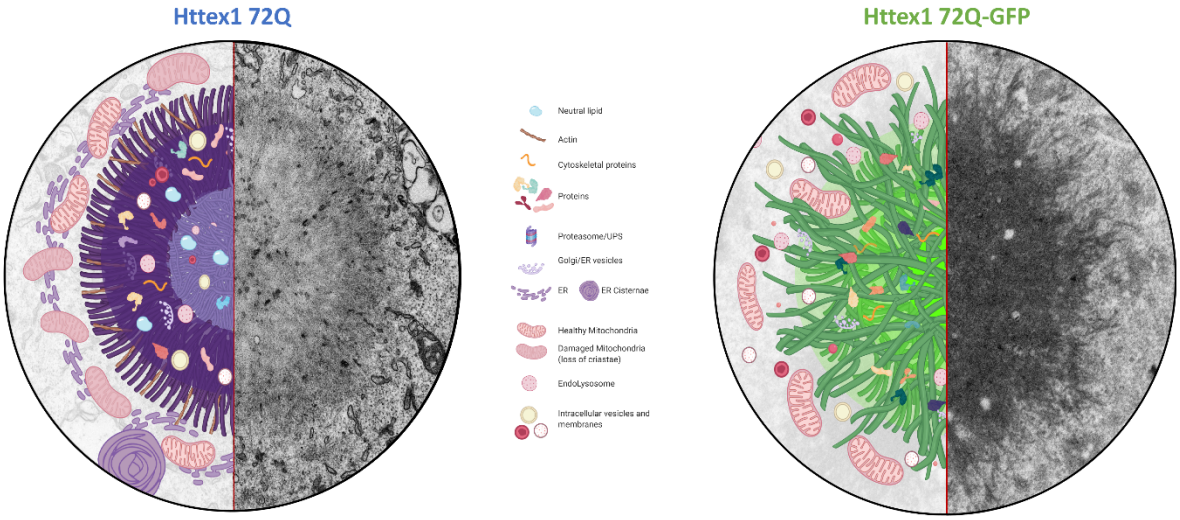

Schematic depictions and original electron micrographs of cytoplasmic inclusions formed by native (tag-free) mutant Huntington exon1 proteins (Httex1 72Q, left) and the corresponding GFP fusion protein (Httex1 72Q-GFP).

Introduction

Huntington's disease (HD) is an autosomal dominant genetic and progressive neurodegenerative disorder caused by the abnormal expansion of CAG trinucleotide repeats within exon 1 of the huntingtin gene (*htt)*[1–4]. The expanded repeats are translated into a long pathogenic polyglutamine (polyQ) tract (>36 repeats) that renders the Huntingtin protein (Htt) more prone to aggregate[5]. The length of the CAG repeat is inversely correlated to the age of onset, with the juvenile form associated with a polyQ repeat length of 75 or more[6,7]. The accumulation of Htt-positive intraneuronal aggregates and inclusions in the cortex and the striatum of *post-mortem* brain from HD patients and in animal and cellular models of HD[2] has led to the hypothesis that Htt aggregation plays a central role in the pathogenesis of HD. However, our understanding of the ultrastructural and biochemical composition of Htt inclusions and the molecular mechanisms that drive their formation, clearance, and toxicity remains incomplete. Addressing this is crucial to understand the molecular and cellular mechanisms underpinning HD and to enable the development of effective therapies and disease-modifying strategies for this disease. Several cellular and animal models of HD have been developed based on the overexpression of mutant N-terminal fragments of Htt. These models reproduce different aspects of Htt aggregation and have been instrumental in advancing our understanding of the sequence, molecular, and structural determinants of Htt aggregation and inclusion formation[8–14].

Although several studies have investigated specific cellular mechanisms linked to Htt aggregation, the current models often lack detailed characterization of the inclusions at both the biochemical and structural levels. Furthermore, while some of the previous studies explored the effect of polyQ repeat on the ultrastructure properties of mutant Htt, there are no reports on the effect of the Nt17 domain on the organization and ultrastructure properties of cytoplasmic and nuclear Htt. Finally, the vast majority of these studies used mutant Htt constructs fused to either peptide-based tags or large fluorescent proteins like GFP that could interfere with the cellular and aggregation properties of Htt[15–18]. Although Tagawa and

colleagues[19] reported on inclusion formation by tag-free mutant Httex1 (111Q) in HeLa cells, they did not provide an in-depth characterization of the ultrastructural properties of the inclusions, and their influence on cellular homeostasis is missing. In another recent study, Bäuerlein and colleagues[15] observed that the addition of GFP leads to an increased stiffness but decreased density of Httex1 fibrils in cellular inclusions, although the constructs used still bore a small peptidic tag.

Here, we employed a cellular model of Htt aggregation and inclusion formation to gain insight into how sequence modifications influence the final ultrastructural and biochemical properties of cytoplasmic and nuclear Htt inclusions and their impact on cellular organelles and functions. The cellular model used here is based on overexpression of N-terminal fragments of mutant Htt comprising the Exon 1 region (Httex1), which contains the polyQ expansion, a key component of the intracellular inclusions found in HD *post-mortem* brains[20–22]. Overexpression of pathogenic Httex1 mutants (polyQ tract > 43Q) is sufficient to induce HD-like features, including the formation of cytoplasmic and nuclear inclusions, behavioral defects, and neurodegeneration in mice[23–25], drosophila[26], and cell culture models[27]. *In vitro* and in cells, Httex1 aggregates in a polyQ repeat length and concentration-dependent manner[28–30]. The first N-terminal 17 amino acids (Nt17) of Htt regulate many aspects of the aggregation and cellular properties of both N-terminal fragments and the full-length Htt protein[12,31–33]. Therefore, mutant Httex1-based models have been used extensively to investigate the role of mutant Htt in the pathogenesis of HD.

We applied *Correlative Light and Electron Microscopy (CLEM)* and proteomics-based approaches to investigate the structural and biochemical properties of the cytoplasmic and nuclear Httex1 inclusions in HEK 293 cells. We also investigated the role of the Nt17 domain and the polyQ tract length in modulating the composition and the structural and toxic properties of mutant Httex1 inclusions. Finally, given that a large body of published cellular studies on the mechanisms of Httex1 aggregation and inclusion formation is based on constructs in which Httex1 is fused to the GFP[32–34], we also compared the composition, ultrastructural properties,

and toxicity of inclusions formed by native (tag-free) and GFP-tagged mutant Httex1. This is the first study to present such a direct comparison and characterization of inclusion formation by tag-free and GFP-tagged mutant Httex1 and their impact on cellular homeostasis.

Our results demonstrate that Htt inclusions are composed of a complex mixture of aggregated mutant Httex1, different cellular proteins, and membranous organelles, including the endosomal system. We show that cytoplasmic and nuclear Htt inclusions exhibit a distinct organization. We demonstrate that functional and ultrastructural properties of Httex1 inclusions are differentially altered by sequence modifications and interactions with lipids and cellular organelles. Finally, we show that inclusions produced by mutant Httex1 72Q-GFP exhibit striking differences in terms of organization, ultrastructural properties, composition, and their impact on mitochondria functions as compared to the inclusions formed by the tag-free mutant Httex1 72Q. These findings highlight the critical importance of developing new tools that minimize the impact of large fluorescent proteins and/or label-free methods for imaging and monitoring Htt aggregation in inclusion formation in cells. Overall, our findings contribute to a better understanding of the sequence, molecular, and cellular determinants of mutant Httex1 aggregation and inclusion formation and underscore the critical importance of further studies to investigate the role that lipids, organelles, and the Htt interactome play in Htt pathology development and Htt-induced toxicity in HD.

Results

Expression of Httex1 72Q in cells leads to the formation of cytoplasmic inclusions with a ring-like architecture

To investigate the ultrastructural properties of Htt inclusions, we used a mammalian cell model system of HD, in which overexpression of mutant Httex1 with polyQ repeats > 39 has been shown to result in a robust and reproducible formation of cytoplasmic Htt inclusions[14,18]. In this model, nuclear inclusions are also observed in ~ 15% of transfected cells by Httex1 72Q (not shown), thus providing an opportunity to investigate and compare the ultrastructural features of cytoplasmic and nuclear Htt inclusions. This model system is widely used to investigate molecular, cellular, and pharmacological modulators of Htt aggregation and inclusion formation[33,35,36], though very often using Htt constructs with extra non-natural sequences such as Myc, FLAG and GFP tags. In this work, we opted to maintain the native sequence of the protein and investigated mutant Httex1 aggregation and inclusion formation in the absence of additional sequences or tags.

Tag-free Httex1 72Q was overexpressed in HEK 293 cells (HEK cells) and the morphology and structural properties of Httex1 inclusions were assessed. To uncouple events associated with inclusion formation from those linked to potential toxic effects of the inclusions, we first assessed the impact of Httex1 72Q on cell viability over time. Despite the formation and abundance of inclusions formed by Httex1 72Q, we did not observe overt toxicity. The initiation of apoptotic events was apparent only after 96h, as indicated by Caspase 3 activation without loss of plasma membrane integrity (not shown).

Next, we assessed the morphology of Httex1 72Q inclusions in HEK cells by immunocytochemistry (ICC) using nine antibodies against different epitopes along the sequence of Httex1 (Figure 1A andS1). Interestingly, all the antibodies presented a strong immunoreactivity to the periphery of the Httex1 72Q inclusions, and none of these antibodies labeled the core of these inclusions (Figure 1B and Figure S2A). This observation suggests either an absence of Htt in the center of the inclusions or poor accessibility of the used antibodies to the core of the inclusions, possibly due to the high compactness of the Htt

aggregates in the core compared to the periphery of the inclusions. In addition, we observed high colocalization of the filamentous actin (visualized by phalloidin) with Httex1 inclusions (Figure 1B, white arrowheads), indicating a possible involvement of the cytoskeleton proteins in Htt inclusion formation.

CLEM of the cytoplasmic Httex1 inclusion reveals a complex structural organization of HTT aggregates and membranous structures, with a distinctive core and shell

To gain more insight into the structural and organizational features of Httex1 inclusions formed in cells, we turned to EM. We first employed a correlative approach to analyze the ultrastructure of the inclusions by EM and their subcellular environment seen with light microscopy—CLEM (Figure 1C and 1D). Httex1 72Q positive inclusions were immunostained and imaged by confocal microscopy (Figure 1C) and then subjected to serial sectioning for analysis by EM (Figure 1D). The EM micrographs of the Httex1 72Q inclusions revealed a surprisingly complex morphology characterized by a halo-like structure with a dense core and a heavily stained outer shell. The outer layer of the inclusions contained fibrillar structures that appeared to be tightly packed and radiating from the core of the inclusion. EM-dense cytoplasmic structures were detected in both the core and the periphery and could reflect the incorporation or sequestration of disrupted organelles inside the inclusion[15,37,38] (Figure 1D, white arrowheads). The halo-morphology of Httex1 inclusions was consistent across several imaged inclusions (Figure S3A).

To further characterize the structural properties and distribution of Httex1 within the inclusion, we used cryo fixation via high pressure freezing (HPF), which preserves the cellular ultrastructure to its native states. EM imaging revealed radiating fibrils at the periphery and more tightly organized and stacked fibrils in the core (Figure S4A). Electron-dense membranous structures were observed in the core and more to the periphery. These results suggest that both the core and shell contain aggregated fibrillar forms of mutant Htt, but with a distinct structural organization. The structural organization of Httex1 72Q inclusions combined with the primary localization of Htt antibodies in their periphery suggest that Htt fibrils in the

outer layer of these inclusions serve as active sites for the recruitment of soluble Htt, the growth of Htt fibrils, and the interaction of Htt with other proteins and cellular organelles.

The cytoplasmic Httex1 inclusions are composed of membranous structures

The ultrastructure of inclusions formed by the Httex1 72Q suggest that their formation is not simply the result of the interactions between Htt monomers but may also involve interactions and the recruitment of other proteins and cellular components. Consistent with this hypothesis, it has been previously reported that Htt intracellular inclusions interact with and/or contain cellular endomembranes, especially of the endoplasmic reticulum (ER)[15] and the mitochondria [18,37,39–41], and alter the organization and functions of these organelles.

To determine whether the formation of cytoplasmic inclusions involves interactions with or recruitment of membranous structures such as ER and mitochondria, we imaged inclusion positive cells by EM under conditions that preserve the internal membranes of cellular organelles, i.e., in the absence of detergents commonly used in the ICC procedure. EM images revealed that the core and periphery of the Httex1 72Q inclusion contained many small membranous structures (Orange arrowheads). An ER network and mitochondria were present at the periphery of these inclusions, suggesting that this region might act as active sites for the recruitment and interaction of soluble Htt with other proteins and cellular compartments during inclusion formation and maturation. Most of the mitochondria surrounding the cytoplasmic Httex1 72Q inclusions exhibited damaged or markedly reduced numbers of cristae (Figure 1E, green arrowheads).

Next, we sought to identify the endomembrane compartments within Httex1 72Q inclusions using a panel of antibodies directed against intracellular compartments. Consistent with the EM results, mitochondrial (Tom 20 and Mitotracker) and ER (BiP/Grp78) markers were strongly detected in close proximity to Httex1 72Q cytoplasmic inclusions (Figure S5A, B, and C). The autophagy flux marker, p62, was enriched in the periphery of Httex1 72Q inclusions, indicating that the autophagolysosomal pathway does not efficiently degrade the inclusions (Figure S5D).

Markers of aggresome formation, such as Vimentin and HDAC6, were enriched in the periphery and in close proximity to Httex1 72Q inclusions (Figure S5E and F). Moreover, when cytoskeletal proteins such as actin and tubulin were overexpressed (fused with RFP), they were observed mainly at the periphery of the Httex1 72Q inclusions (Figure S5G and H). This observation is consistent with the colocalization of F-actin (stained by phalloidin) with Httex1-72Q inclusions (Figure 1B, white arrowheads). Although the EM images clearly showed the presence of membranous structures inside the core of the Httex1 72Q inclusions (Figure 1E), none of the organelles' markers were detected inside the core of these inclusions (Figure S5). Even using fluorescently tagged markers for actin or tubulin and the Mitotracker, the fluorescent signal was mostly localized in the outermost region of the inclusions (Figure S5). These results favor the hypothesis that proteins and organelles are excluded or not recruited into the core of the inclusions or that early events associated with the formation of the aggregates in the core are driven by purely mutant Httex1 aggregation. The periphery of the Httex1 inclusions is composed of less tightly packed filaments and may act as an active zone for the interaction and/or recruitment of proteins and cellular compartments during the formation and maturation of the inclusions.

3D reconstruction of Httex1 inclusions indicates perturbation of the ER organization

To further investigate the structure of Httex1 inclusions and their impact on cellular compartments, we generated a 3D model of the inclusions and the organelles in their vicinity. In cells containing Httex1 72Q inclusions, serial EM images were captured, aligned, and the different features segmented (Figure 1E). These segmentations were then used to create a 3D model of the inclusion and surrounding cellular components (Figure 1F). This model showed that the inclusion formed in a crowded region with the presence of ER and mitochondria all around it. The 3D model suggests that the electron-dense membranous structures recruited inside the Httex1 inclusions were mostly composed of endomembranes and vesicles (labeled in white), consistent with a previous report[15,37]. Interestingly, the ER adopted a specific "rosette-like" or "stacked cisternae" morphology (highlighted by a red

arrowhead) in the periphery of some Httex1 72Q inclusions. Finally, it is noteworthy that the mitochondria (labeled in yellow) were not detected inside the inclusion but rather at the periphery of the inclusions. Interestingly, despite the proximity of the cellular inclusions to the nucleus, the inclusion did not compromise the nuclear membrane integrity (Figure S3A).

Cytoplasmic and nuclear Httex1 inclusions exhibit distinct ultrastructural properties

Both cytoplasmic and nuclear inclusions have been observed in HD patients' brains and transgenic mouse models of HD[42–44]. We hypothesized that the differences in the cellular environment and interactome could influence the mechanisms of aggregation, the structural and biochemical properties of the inclusions, and their relative contribution to mutant Htt-induced toxicity. Therefore, we sought to compare the structural and organizational properties of Httex1 72Q inclusions in the cytoplasm (~85%) and nucleus (~15%) of the transfected HEK cells containing inclusions. Using immunofluorescence-based confocal microscopy, we did not observe significant differences in the size or overall morphology between the Httex1 72Q inclusions in the nucleus or the perinuclear region (Figure S6A). However, EM clearly showed that the subcellular location dramatically influences the ultrastructural properties of the inclusions formed by Httex1 72Q inclusions (Figure S6B). The nuclear inclusions formed by the Httex1 72Q were also enriched in fibrillar structures but did not exhibit the classical core and shell organization observed for the cytosolic inclusions (Figure 1D and E), nor did they contain the membranous structures trapped within the cytosolic inclusion. This suggests that the intracellular environment is a key determinant of the structural and molecular complexity of the inclusions and that nuclear and cytosolic inclusion formation occurs via different mechanisms. Although previous studies have suggested the formation of ring-like nuclear inclusions, this architecture was defined by the peripheral staining of nuclear proteins and not by the peripheral staining of Htt as observed in the case of cytoplasmic inclusions (Figure 1).

The length of the polyQ domain is another key determinant of inclusion formation

We and others have previously shown that the polyQ repeat length strongly influences the conformation and aggregation properties of Httex1, with higher polyQ favoring the formation of a more compact polyQ domain and accelerating Htt aggregation *in vitro* and *in vivo*[30,45,46]. However, the polyQ dependence on Htt inclusion formation has predominantly been assessed in the context of Htt fused to fluorescent proteins and polyQ repeats much higher than the pathogenic threshold (64Q-97Q[15]; 64Q-150Q[47]; 43Q-97Q[17]). Therefore, we next explored whether the length of the polyQ repeat also influences the organization and ultrastructural properties of cytoplasmic and Htt inclusions in HEK cells. Toward this goal, we investigated the level of aggregation and the structural organization of the Httex1 inclusions carrying different polyQ lengths (16Q, 39Q vs 72Q). No significant cell death was observed in HEK cells overexpressing Httex1 16Q or 39Q constructs even after 96h (not shown). However, cells expressing Httex1 72Q underwent apoptosis after 96h. We observed a direct correlation between polyQ length and the extent of mutant Htt cellular toxicity. As expected, no inclusions were formed upon overexpression of Httex1 16Q even after 72h post-transfection (Figure S7). Httex1 39Q inclusions were detected predominantly in the cytoplasm of the HEK cells at all the time points examined (24-72h), though at lower numbers than in the Httex1 72Q conditions: Httex1 39Q (16%) vs Httex1 72Q (38%) of transfected cells (not shown).

Characterization of the inclusions by EM revealed that the polyQ tract length dramatically influences the ultrastructure properties of the Httex1 inclusions. The dark shell structure that delimitated the core from the periphery of the Httex1 72Q inclusions (Figures 1D and E) was absent in the Httex1 39Q inclusions (Figure 2A). In addition, the Httex1 39Q inclusions appeared less dense compared to that of the Httex1 72Q. These observations were consistent for all eight inclusions imaged per condition (Figure S3B).

Similar to what we observed for Httex1 72Q, the 3D reconstruction of the Httex1 39Q inclusions clearly showed alteration of the ER organization, as well as the localization of mitochondria near the inclusions (Figure 2B). The electron-dense membranous structures found inside the inclusions were identified as endomembranes and vesicles. Httex1 39Q expressing cells also contained specific ER-cisternae at the periphery of the inclusions (red arrowheads, Figure 2B).

Altogether, our data establish that polyQ expansion plays a critical role in shaping the architecture and ultrastructural properties of the Httex1 inclusions.

Removal of the Nt17 domain reduces aggregation formation and toxicity but does not influence the organization and ultrastructural properties of the inclusions

The Nt17 domain functions as a Nuclear Export Signal (NES) and has been shown to play an important role in regulating the intracellular localization of Htt as well as its kinetics of aggregation and extent of inclusion formation[13,48]. Therefore, we sought to assess the role of Nt17 in regulating the ultrastructural properties of Htt inclusions. Towards this goal, we generated Httex1 39Q and 72Q mutants lacking the entire Nt17 domain (ΔNt17) and compared the structural properties of the inclussions formed by these mutants to those formed by Httex1 39Q and Httex1 72Q. Quantitative confocal microscopy revealed a strong reduction in the number of inclusions (~50% reduction) of cells transfected by Httex1 ΔNt17 72Q compared to Httex1 72Q (data not shown). Surprisingly, inclusions formed by the Httex1 ΔNt17 72Q (Figure 2C) exhibited an architecture and organization (central core and peripheral shell) similar to those formed by Httex1 72Q (Figure 1D-E and Figure S8A). Similar to Httex1 39Q, the Httex1 ΔNt17 39Q cytoplasmic inclusions did not exhibit a core and shell architecture. These observations suggest that the Nt17 domain—while playing a crucial role in regulating the kinetics and early events of Htt aggregation—does not influence the morphology or structural organization of Htt inclusions.

Neutral lipids are incorporated into Httex1 cellular inclusions in a polyQ length-dependent manner

Recent studies showed that the formation of pathological inclusions, Lewy bodies in Parkinson's disease, involves the recruitment of lipids and membranous organelles[49,50]. Although several studies have shown dysfunction of cholesterol metabolism in various cellular and animal models of HD, the role of lipids in Htt inclusion formation and the lipid composition of cellular huntingtin inclusions remains unknown[51,52]. To gain further insight into the role that

lipids play in the formation and structural organization of Httex1 inclusions, we next assessed their presence using fluorescent probes targeting different lipid classes. We did not observe the recruitment of ceramide, cholesteryl ester, and phospholipids into mutant Httex1 inclusions (Figure S9 A-C). However, neutral lipids were found to be enriched in the center of Httex1 72Q inclusions (Figure S9E, white arrowheads) but not in Httex1 39Q inclusions (Figure S9D). Neutral lipids were also detected in nuclear inclusions (Figure S11E, yellow arrowheads). Although the Nt17 domain has been shown to act as a lipid-binding domain and membranes, neutral lipids were also detected in the Httex1 ΔNt17 72Q inclusions, though not inside Httex1 ΔNt17 39Q inclusions (Figure S10A). These results demonstrate that polyQ-dependent interaction between Htt and neutral lipids play important roles in Httex1 aggregation and the formation of both nuclear and cytoplasmic inclusions. Interestingly, these interactions are not dependent on the Nt17 domain, which has been reported to interact with membranes and phospholipids. Finally, these mechanisms could potentially contribute to the differences in the ultrastructural properties of the Httex1 39Q and Httex1 72Q inclusions (Figures 1E and 2A).

Quantitative proteomics reveals that the formation of Httex1 72Q inclusions involves the active recruitment and sequestration of proteins and organelles

Our EM studies combined with 3D reconstructions showed that the formation of Httex1 72Q inclusions is accompanied by the sequestration of disrupted ER and vesicles inside the inclusion while its periphery is surrounded by mitochondria and membranous organelles. To gain further insight into the biochemical composition of Htt inclusions, and the molecular interactions and mechanisms that govern their formation and maturation, we investigated the proteome of Httex1 72Q inclusions. Toward this goal, we first established a detergent fractionation protocol to isolate strongly insoluble proteins due to the formation of Httex1 inclusions in HEK cells, 48h post-transfection. Httex1 inclusions were isolated using ultracentrifugation and dissolved using Sarkosyl supplemented by 8M urea and sonication. Western Blot (WB) analysis of the urea fraction confirmed the presence of Httex1 72Q due to

the formation of insoluble inclusions, while non-pathogenic Httex1 16Q was not present in the urea fraction (Figure S11A). We then performed quantitative proteomic analysis and compared the proteins that were differentially expressed between the urea insoluble fractions of HEK cells overexpressing Httex1 72Q or Httex1 16Q (see experimental details, Figure S11A).

The volcano plot shown in Figure 3A is the result of three independent experiments (FDR <0.05 and S0 of 0.5). First, we showed that no proteins were significantly enriched in the insoluble fraction of HEK cells expressing Httex1 16Q compared to that expressing GFP (Figure S11C). This is in line with our previous findings showing that Httex1 16Q overexpression does not result in the formation of inclusions (Figure S7). Our analysis showed that 377 proteins were significantly enriched in the insoluble fraction of HEK cells overexpressing Httex1 72Q compared to that in cells overexpressing Httex1 16Q (Figure 3A). Among these proteins, we identified the endogenous HTT protein (Figure S11E). This suggests that the aggregation process triggered by the overexpression of Httex1 also leads to the recruitment of endogenous HTT protein. The Gene Ontology (GO) term analysis combined with the database for annotation, visualization, and integrated discovery (DAVID) analysis was used to classify these proteins by cellular component (Figure 3B) and biological process (Figure 3C). Upregulated signaling pathways were investigated using the Ingenuity Pathway Analysis (IPA) (Figure S12).

Classification by cellular component (CC, Figure 3B) showed that 55 % of the proteins enriched in the insoluble fractions of HEK cells containing Httex1 72Q inclusions were part of the cytoplasmic compartment, with 24% of these proteins belonging to the endomembrane system including the endolysosomal apparatus (clathrin-coated endocytotic vesicles, early endosome, endosomes, recycling endosomes, exosomes, and autophagosomes), the vesicles involved in Golgi-ER transport, and membranes from the Golgi and trans-Golgi network. These data are in line with the EM data showing that the Httex1 72Q inclusions were composed of small membranous structures and vesicles. Approximately 14% of the proteins enriched in the insoluble fraction were classified as pertaining to the cytoskeleton compartment, with the actin cytoskeleton being the most predominant in terms of this classification, consistent with our

confocal results (Figure 1B). The absence of mitochondria proteins in the urea insoluble fraction confirms that mitochondria are not sequestered inside the inclusions but, rather, accumulate at the periphery, as shown by our EM imaging. The rest of the cytoplasmic proteins sequestered in the insoluble fraction of the Httex1 72Q-transfected HEK cells were mainly from the perinuclear region, or were part of macromolecular protein complexes such as the ubiquitin-proteasome system (UPS), the mRNA processing bodies, and the stress granules. Interestingly, the insoluble fraction of the Httex1 72Q-transfected HEK cells was also significantly enriched by proteins from the nuclear compartment (~ 45%). Among the nuclear proteins, ~ 71.6% belonged to the nucleoplasm. Proteins from the nucleolus, the nuclear bodies, the nuclear envelope, and the nuclear pore were also significantly enriched.

To better understand how the sequestration of functional proteins during the process of Httex1 72Q inclusion formation and maturation could impact the biological functions of the cells, we next classified the proteins enriched in the Httex1 72Q-transfected HEK by biological process (Figure 3C) and signaling pathways (Figure S12). In line with the cellular compartment analysis, our proteomic data showed that the most highly enriched terms for the biological process and the signaling pathways were related to the proteins involved in the proteasomal ubiquitin-dependent protein degradation. In addition, proteins related to the chaperone machinery (e.g., DNAJB6, DNAJB2, and other proteins from the Hsp40 and Hsp70 families) were enriched in the insoluble fraction of the HEK cells with Httex1 72Q inclusions. This cluster of proteins was associated with the BAG2 signaling pathway (Figure S12), one of the top canonical signaling pathways that regulates the interplay between the chaperones from the Hsp70/Hsc70 family and the ubiquitin. Altogether, our data suggest that the formation and maturation of the Httex1 72Q inclusions are accompanied by the sequestration of the proteins involved in the degradation machinery and the protein quality control pathway. This might potentially result in the failure of the protein degradation machinery to clear off the Httex1 72Q inclusions.

Our proteomic analysis also revealed the enrichment of several biological processes and signaling pathways related to RNA binding proteins, transcription factors, RNA splicing, mRNA processing, and stability, as well as chromatin and nucleotide binding proteins (Figure 3C and Figure S12). Dysregulation of transcriptional gene pathways has been reported in several animal and cell HD models[53–55] as well as in HD post-mortem tissues and HD peripheral blood cells[56–58]. Our findings support the hypothesis that sequestration of the key regulators of transcription inside the Htt inclusions could be one of the causative mechanisms of transcription dysregulation in HD.

Finally, several signaling pathways and biological processes related to toxicity, oxidative stress, and inflammation responses were upregulated in the HEK cells with Httex1 72Q inclusions (Figure 3C and Figure S12). These include Huntington's disease signaling and several apoptosis processes, such as death receptor signaling and TWEAK signaling, but also the iNOS and the oxidative stress signaling pathways. The inflammation signaling pathways, such as Toll-like receptor signaling, interleukins signaling, and NFκB signaling were among the top canonical pathways shown as upregulated in the insoluble fraction containing the Httex1 72Q inclusions. Oxidative stress and inflammation responses are closely interrelated and have been suggested to be key players in disease progression for HD and neuronal dysfunctions. Together, our proteomic and CLEM data provide strong evidence that the formation of the Httex1 72Q inclusions does not occur simply through the assembly of misfolded Httex1 but instead involves the active recruitment and sequestration of cellular proteins, lipids, and organelles.

Httex1 72Q inclusion formation induces mitochondrial fragmentation and increases mitochondrial respiration

The remarkable accumulation of damaged mitochondria at the periphery of Httex1 72Q inclusions in all electron micrographs and 3D reconstructions prompted us to investigate how

Htt inclusion formation impacts mitochondrial functions. Quantification of mitochondrial length from EM-micrographs revealed a shorter mitochondrial profile associated with Httex1 72Q inclusions, as compared to HEK cells transfected with empty vector (Figure 4B). Similar levels of the outer mitochondrial membrane protein VDAC1 suggest that this mitochondrial fragmentation was not associated with a decrease in mitochondrial density (Fig. S13D). We hypothesized that the fragmentation and recruitment of mitochondria to Httex1 inclusions might be associated with respirational dysfunction. Therefore, we performed high-resolution respirometry on cells transfected with Httex1 16Q and 72Q for 48h (for setup, see Figure S13A). Mitochondrial respiration was assessed in different respirational states (Figure S13B). Httex1 72Q transfection resulted in significantly higher mitochondrial respiration than Httex1 16Q transfection in the different respiration states (Figures 4C). Overall, our results demonstrate a clear effect of Httex1 72Q inclusion formation on mitochondrial morphology and function.

Formation of Httex1 inclusions leads to ER-exit site remodeling

Our EM analysis and 3D reconstruction also revealed the presence of ER cisternae at the periphery of the Httex1 inclusions. Stacked ER cisternae are usually formed by an increasing concentration of specific resident proteins or stress conditions[59]. The changes we observed in ER organization, together with the enrichment of proteins related to ER-Golgi trafficking inside the inclusions, prompted us to investigate whether ER functions were impaired upon the formation of the Httex1 inclusions.

A major function of the ER is the biogenesis of COPII carriers that ferry proteins and lipids to distal compartments. COPII carriers form at ER exit sites (ERES), which are ribosome-free domains of the rough ER. To determine whether the formation of Httex1 inclusions interferes with the homeostasis of the ERES, we used confocal imaging and quantified the number of ERES, labeled specifically by the COPII component Sec13 protein in HeLa cells expressing

Httex1 72Q, Httex139Q, or Httex1 16Q (Figure 5). Our data show that the number of ERES was significantly reduced (~ 20%) only in cells containing Httex1 72Q inclusions (Figure 5B, upper panel). We next quantified the size of the ERES using the same imaging pipeline (Figure 5B, lower panel). Overexpression of Httex1 16Q caused a 20% reduction in the size of the ERES compared to EV. However, the reduction became much more significant in the cells carrying Httex1 39Q or Httex1 72Q, with a ~40% decrease compared to EV and ~20% compared to Httex1 16Q. These results demonstrate that the formation of the Httex1 inclusions interferes with the formation and fusion of ERES. The remodeling of ERES in cells has been described primarily as an adaptive response to the protein synthesis level of ER with the number of ERES proportional to the cargo load. Interestingly, our proteomics results (Figure 3A) showed that the TGF (Transforming Growth Factor) protein—which plays a central role in the biogenesis and organization of ERES—is sequestered in mutant Httex1 inclusions[60]. In line with our results, it has been previously shown that the depletion of TGF induced a dramatic reduction of the ERES sites[61]. Alternatively, the reduction of the ERES sites could represent early signs of cell vulnerability and toxicity induced by the presence of the Httex1 inclusions in cells.

The addition of GFP to the C-terminal part of Httex1 induces a differential structural organization revealed by CLEM

Given that the great majority of cellular models of HD rely on the use of fluorescently tagged Htt constructs, we next investigated the aggregation properties of mutant Httex1 fused to GFP (Httex1 72Q-GFP and Httex1 39Q-GFP). First, we assessed the morphology of Httex1 72Q-GFP inclusions in HEK cells by immunocytochemistry (ICC) using a panel of Httex1 antibodies (Figure 6A). Confocal imaging revealed a diffuse GFP signal throughout the inclusions. Conversely, the Htt antibodies labeled mainly the outermost region of Httex1 72Q-GFP inclusions, but also faintly stained the center of the Httex1 72Q-GFP inclusions (Figure 6B) unlike the tag-free inclusions cores, which were not labeled by all the Htt antibodies tested.

Thus, we hypothesized that the presence of the GFP tag results in the formation of less compact Httex1 inclusions. While Actin-F was found to be localized at the periphery of tag-free Httex1 72Q inclusions (Figure 1B), no specific enrichment Actin-F was detected in the core or periphery of the Httex1 72Q-GFP inclusions.

Next, we performed a more in-depth analysis of Httex1 72Q-GFP cellular inclusions by CLEM (Figure 6C and 6D). The Httex1 72Q-GFP inclusions were organized as a highly dense network of fibrils, which were more homogenously stained (Figure 6D) and did not exhibit the core and shell architecture that is characteristic of the tag-free Httex1 72Q inclusion (Figure 1D). Closer examination of the inclusions showed that they were composed of densely packed fibrils that exhibited a striking resemblance to the fibrillar aggregates formed by mutant Httex1 proteins in a cell-free system (Figure S14B). Structural analysis of Httex1 72Q-GFP by HPF fixation (Figure S4B) also revealed densely packed fibrils radiating from the inclusions. The center of the inclusions was not well resolved, but thicker fibrils could clearly be observed radiating at the periphery with increased spacing between them compared to tag-free Httex1 72 inclusion (Figure S4A)

A portion of Httex1 72Q-GFP inclusions exhibited perinuclear localization. In some cases, the accumulation of fibrils near the nuclear membrane leads to apparent distortion of the nucleus, but without membrane disruption (Figure 6D and S15A). Overall, we observed no significant differences in diameter and distance from the nucleus for all the Httex1 (+/-GFP) inclusions imaged in our system (Figure S16).

Next, we investigated the ultrastructure properties of Httex1 72Q-GFP inclusions present in the nucleus (Figure 6E and 6F). No significant differences in terms of organization were observed between nuclear and cytoplasmic Httex1 72Q-GFP inclusions by both GFP detection and antibody staining (Figure 6E). The Httex1 72Q-GFP nuclear inclusions were also enriched in fibrillar structures. The 3D reconstruction generated from the series of electron micrographs revealed much fewer membranous structures in both Httex1 39Q-GFP and Httex1 72Q-GFP inclusions (Figure S17) compared to tag-free Httex1 inclusions (Figure 1F and 2B). Moreover,

consistent with EM observations, no neutral lipids were found in Httex1 39Q-GFP and Httex1 72Q-GFP inclusions (Figure S10B). To compare Httex1 inclusions having a similar fluorescent tag as GFP to the exact same neutral lipid stain as that for tag-free Httex1 inclusions, we took advantage of Httex1 72Q-mCherry (red fluorescence) that also did not show lipid enrichment (Figure S10C).

Interestingly, neither the length of the polyQ repeat nor the presence or removal of the Nt17 domain seem to significantly alter the size morphology or structural properties of the inclusions by mutant Httex1 proteins fused to GFP (Figure S18). This is different from what we observed for cells expressing tag-free Httex1, in which the increase of the polyQ length led to inclusions with distinct morphologies and organizational features and in which cytoplasmic inclusions were enriched in membranous structures. These findings suggest that the addition of GFP significantly alters the mechanism of Httex1 aggregation and inclusion formation.

Next, we performed EM under detergent-free conditions to preserve the internal membranes and structures of the inclusions. We observed that the length of the polyQ repeat did not influence the size of the Httex1 39Q-GFP and 72Q-GFP inclusions (Figures S17A and S17B) or their overall architecture. The Httex1 39Q-GFP inclusions are composed of radiating fibrils and are thus similar to—although slightly less dense than—that observed for the Httex1 72Q-GFP inclusions.

The 3D reconstruction of the inclusions showed the presence of ER and mitochondria in their periphery, but few membranous structures were internalized (yellow arrowhead, Figures S19) as compared to tag-free Httex1 39Q and Httex1 72Q inclusions. A similar analysis of Httex1 ΔNt17 39Q-GFP and Httex1 ΔNt17 72Q-GFP inclusions (found in cells) (Figure S18) also revealed no effect of Nt17 deletion on the ultrastructure of the inclusions or their interactions with the surrounding organelles. These results confirm that the mechanism of aggregation and inclusion formation is different and significantly altered by the addition of the GFP.

The Httex1 72Q and Httex1 72Q-GFP inclusions exhibit distinct proteome composition

To further assess the similarities and differences in the proteome composition of cellular Httex1 inclusions formed by the tag-free and GFP mutant Httex1-72Q, we performed quantitative proteomic analysis of the insoluble fractions from lysates of cells expressing these constructs (see experimental workflow, Figure S11A). Volcano plot analysis showed the 492 proteins significantly enriched in the insoluble fraction of the HEK overexpressing Httex1 72Q GFP as compared to those expressing GFP (Figure 7A). We observed a significant enrichment of the endogenous HTT protein, suggesting that, as for the tag-free Httex1 72Q, mutant Httex1-GFP inclusions can recruit the endogenous Htt protein (Figure S11E).

The cytoplasmic components enriched in the insoluble fraction of Httex1 72Q-GFP were similar to those found with tag-free Httex1-72Q and were part of the endomembrane system (~50%, light blue Figure 7B), the cytoskeleton, the perinuclear region, the UPS, mRNA processing bodies, and stress granules (dark blue Figure 7B). However, in contrast to the tag-free Httex1 72Q insoluble fractions, in which no mitochondrial protein was found to be enriched, 10% of the proteins enriched in the Httex1 72Q GFP insoluble fraction were related to the mitochondria compartment (purple Figure 7B). The nuclear proteins found in the Httex1 72Q GFP insoluble fraction belong to similar nuclear compartments as those identified previously in the Httex1 72Q insoluble fraction (grey Figure 7B).

Biological process (Figure S19) and canonical pathway (Figure S20) analyses revealed that proteins related to the UPS and chaperone machinery were the most enriched terms, as previously observed in the tag-free insoluble fraction. This indicates that the process of aggregation of Httex1 itself, regardless of the presence of the GFP tag, leads to the sequestration of the key cellular machinery responsible for protein folding and protein degradation. This could compromise the cell's ability to prevent the accumulation or clearance of Httex1 aggregates. Although in different proportions, most of the biological processes and

pathways significantly enriched in the tag-free Httex1 72Q insoluble fraction, such as inflammation, transcription, Huntington's disease signaling, and cell death, were also detected in the Httex1 72Q GFP insoluble fraction.

Having identified the proteins significantly enriched in both tag-free and GFP-tag 72Q inclusions, we next determined which proteins were unique to each type of inclusion. Toward this goal, we used a Venn diagram to compare our list of proteins significantly enriched in our volcano plot analyses [(Httex1 72Q vs Httex1 16Q insoluble fractions) vs (Httex1 72Q GFP vs Httex1 16Q insoluble fractions)] (Figure 3A and Figure S11D). Figure 7C shows that ~45% (256 proteins) were found in both the tag-free or the GFP-tag Httex1 72Q inclusions. In total, 120 proteins (20.9%) were unique to the Httex1 72Q insoluble fraction and 198 proteins (34.5%) were unique to the Httex1 72Q GFP. Overall, we found 55% different proteins among the proteins that co-aggregate with or are sequestered in Httex1 72Q vs 72Q-GFP inclusions, both compared to Httex1 16Q. We used the Kyoto Encyclopedia of Genes and Genomes (KEGG) pathway analysis to classify the list of proteins in Httex1 inclusions (Figure 7D). The proteasome, protein processing in endoplasmic reticulum, and endocytosis were among the most enriched pathways from the common co-aggregated proteins. Those three terms were also enriched significantly for Httex1 72Q-GFP, indicating the involvement of other unique proteins enriched in those pathways compared to Httex1 72Q. The KEGG classification revealed two distinct clusters for Httex1 72Q and Httex1 72Q-GFP, as well as additional differences (Figure 7D). Proteins related to infection and inflammatory pathways (e.g., Herpes simplex infection, TNF signaling, and Toll-like receptor signaling) were found to be unique to Httex1 72Q, whereas proteins related to the metabolism were specifically enriched for Httex1 72Q-GFP. Our proteomic analysis highlights that the addition of a fluorescent tag such as GFP alters significantly not only the mechanim of Htt inclusion formation but also the Htt interactome and thus the biochemical cmposision of inclusions.

Httex1 72Q inclusions induce higher respirational dysfunction and a stronger decrease of ERES number compared to Httex1 72Q-GFP

Next, we investigated the effect of mutant Httex1-GFP inclusion formation on mitochondrial and ER-related functions. Mitochondrial respiration in different respirational states was assessed (Figure S13A and B). Compared to our findings with the tag-free mutant Httex1-72Q (Figure 4C), the increased mitochondrial respiration was significant but less pronounced for Httex1 72Q-GFP as compared to Httex1 16Q-GFP (Figure S13C). Given the role of mitochondria as a major source of reactive oxygen species (ROS), with implications of ROS in both neurodegenerative disease and cellular protective signaling cascades[62,63], we suspected that mitochondrial ROS production might be affected by the mitochondrial fragmentation observed in regions close to tag-free Httex1 72Q and absent for Httex1 72Q-GFP (Figures S21A and B). To test this hypothesis, we used an amplex red assay to measure mitochondrial ROS (superoxide and hydrogen peroxide) production concurrent with mitochondrial respiration (Figure S13B). We observed no significant differences in mitochondrial ROS production between the tag-free or GFP tagged Httex1 72Q or 16Q (Figure S21C).

We also investigated whether Httex1-GFP inclusions interfere with the homeostasis of ERES. We expressed the different GFP-tagged Httex1 mutants in HeLa cells and compared them to cells expressing Httex1 16Q-GFP (Figure S22A). We found that cells containing Httex1 72Q-GFP inclusions caused a decrease in ERES number (Figure S22B, upper panel), although non-significant, contrary to Httex1 72Q, which showed a 20% reduction (Figure 5B, upper panel). The reduction of ERES size was significant for cells expressing Httex1 72Q-GFP but not Httex1 39Q-GFP compared to Httex1 16Q-GFP. (Figure S22B, lower panel). The effect of Httex1-GFP inclusions on ERES is present but less pronounced than what we observed for cells having tag-free Httex1 inclusions.

Overall, the cellular organelle responses and adaptation to inclusion formation were different for the Httex1 72Q-GFP inclusions compared to the Httex1 72Q inclusions, consistent with our

GFP-dependent changes observed in the proteome of and ultrastructural properties of Httex1 inclusions.

Discussion

The detection of Htt aggregates and inclusions in HD brains, combined with the increased aggregation and inclusion formation by mutant forms of full-length and various N-terminal Htt fragments, led to the hypothesis that Htt aggregation and inclusion formation play a central role in the pathogenesis of HD. However, the exact mechanisms of Htt aggregation and inclusion formation in the brain and how these processes contribute to the initiation and progression of HD remain unknown. To address this knowledge gap, several animal and cellular models of HD have been developed, based mostly on overexpression of full-length or N-terminal fragments of Htt bearing an expanded polyQ tract of 46 to 160Q[14,35,64,65]. These HD models show robust aggregation and inclusion formation [24,66–69]. Cellular and neuronal models of HD provide several key advantages for investigating the mechanisms of Htt aggregation and inclusion formation, as they allow for 1) dissecting the key molecular and cellular events associated with these processes using advanced electron microscopy and imaging techniques; and 2) a more direct assessment of how modifying Htt aggregation and inclusion formation alters cellular functions and viability using a combination of proteomics, transcriptomics, and functional studies. This is illustrated by the recent application of electron tomography techniques, to gain insight into the ultrastructural properties of Htt inclusions and how they interact with cellular organelles and influence their functions. In this work, we expanded on these studies and provided new insight into 1) the sequence determinants (polyQ repeat length and the role of the Nt17 domain) of Htt aggregation and inclusion formation; 2) the impact of different types of Htt inclusions on the structural and functional properties of cellular organelles; and 3) the role that the cellular environment plays in determining the biochemical composition and ultrastructural properties of cytoplasmic and nuclear Htt inclusions. Finally, we provided a more in-depth analysis of the impact of fluorescent fusion proteins (GFP), which are commonly used to investigate the mechanisms of Htt inclusion formation and toxicity, on the biochemical and ultrastructural properties of Htt inclusions and their impact on cellular components and organelles.

Our detailed analyses of the ultrastructure of the Httex1 72Q inclusions by CLEM and detergent-free EM revealed their fibrillar nature but also showed a previously unreported core and shell structural organization for mutant Httex1 inclusions. Additionally, we showed that Httex1 72Q is composed of highly organized radiating Htt fibrils that are densely packed at the core compared to the periphery where the fibrils remain highly organized but less densely packed. The periphery of the inclusions is decorated by membranous organelles and cytoskeletal proteins (Figure 1). The formation of this complex organization of the Httex1 inclusions was strongly dependent on the length of the polyQ repeat (Figure 2A) but not on the Nt17 domain (Figure 2C). Finally, our quantitative proteomic analysis showed that the formation and maturation of inclusions are accompanied by the sequestration of proteins related to some of the major cellular pathways that are dysregulated in HD[70,71], such as the inflammation and transcriptomic pathways as well as the quality control machinery, including the ubiquitin-proteasome system, the autophagy pathway, and the chaperones related to protein folding and proteostasis (Figure 3). Altogether, our findings suggest that the formation of Huntingtin inclusions is driven primarily by the polyQ repeat domain and involves the active recruitment and sequestration of lipids, proteins, and membranous organelles. The periphery of the Httex1 inclusion might act as an active site for Htt fibril growth and for the interaction of the radiating Htt fibrils with the cellular compartments, leading to an alteration of the organization and functions of these organelles, which could ultimately contribute to cellular dysfunction and neurodegeneration.

Httex1 inclusion formation and maturation involves a complex interplay between Httex1 aggregates and organelles

Pathological inclusions in neurodegenerative diseases have been shown to have a complex organization and composition. In Parkinson's disease (PD), it has been recently shown that Lewy bodies (LB) isolated from PD brains or LB-like inclusions in primary neurons are

composed of not only filamentous and aggregated forms of alpha-synuclein but also a complex milieu of lipids, cytoskeletal proteins, and other proteins and membranous organelles, including mitochondria and autophagosomes[49,50,72,73]. Studies in neuronal cultures also showed that the recruitment of lipids and membranous organelles during LB formation and maturation contribute to organelles' dysfunctions and lead to synaptic dysfunction and neurodegeneration. In line with these findings, our EM data, together with 3D reconstruction, revealed the presence of fragments of membranes and vesicles entrapped in the core of the Httex1 inclusions. This is consistent with our proteomic analysis, which revealed that 24% of the proteins enriched in the inclusions fraction belong to the endolysosomal apparatus, and the Golgi and the trans-Golgi network (Figure 3). In addition, the periphery of the inclusions was decorated with mitochondria and ER, as previously reported for the Htt inclusions in cellular models[18] and human tissue[74,75]. We hypothesized that sequestration of key functional proteins, together with endomembranes and organelles inside the Httex1 inclusions, could challenge the cellular homeostasis. In line with this hypothesis, our electron micrographs revealed that the mitochondria associated with Httex1 72Q inclusions were fragmented and often exhibited disorganized or depleted cristae (Figure 4A). These changes in mitochondria morphology were associated with dysregulation of the mitochondria respiration (Figure 4), consistent with previous studies demonstrating that mutant Htt aggregates interact directly with outer mitochondrial membranes (in STHdh cells)[76] and induce mitochondrial fragmentation (in primary neurons)[77]. Defects in mitochondrial respiration have also been observed in HD patients' brains, especially for the complex II and IV of the respiratory chain resulting in an impaired oxidative phosphorylation[78–80].

The ER at the periphery of the Httex1 72Q inclusions were also affected at the structural level, as shown by their morphological reorganization in rosette or "stacked cisternae", and at the functional level as is evident from the dysregulation of the ERES homeostasis (Figure 5). Formation of ER rosettes indicates the accumulation of proteins in the smooth ER[59] and is thought to be the result of low-affinity binding and export defects, which can be caused by

unfolded Htt proteins but is not necessarily linked to ER stress. The formation of Httex1 inclusions seems to drive the reorganization of the ER network in their periphery but did not lead to ER protein sequestration, as shown by the quantitative proteomic analysis, which did not reveal significant ER proteins trapped inside the inclusions. The presence of ribosomes and ER membrane deformation was previously detected close to the periphery of Httex1 inclusions by cryo-ET[15] and was linked to a strong reduction in ER dynamics. In the same study[15], the periphery of the inclusions was immunoreactive to several components of the ER-associated degradation (ERAD) machinery (e.g., Erlin-2, Sel1L). These observations are consistent with our ICC data showing the presence of ER chaperone BIP at the outer periphery but not inside the inclusions (Figure S5). We also observed ERES modulation, which can be explained by the sequestration of specific proteins required for their fusion[81]. Indeed, our proteomic analysis showed the enrichment of proteins specific to the ER-Golgi trafficking. ERES modulation can also be explained by a reduction of the biosynthetic capacity of this compartment, as ERES have been shown to adapt to the amount of secretory burden to which they are exposed[82]. The recruitment and perturbation of the ER network might contribute to cytotoxicity during inclusion formation. Consistent with this hypothesis, ERAD and Ca^{2+} signaling have been extensively reported to be dysregulated in various cellular and animal models using different Htt fragments[83–88].

Cytoplasmic and nuclear Htt inclusions exhibit distinct ultrastructural properties that are differentially influenced by the size of the polyQ repeats

Our in-depth characterization of the Httex1 72Q inclusions at the ultrastructure level revealed distinct differences in the organization and architecture between the cytoplasmic and nuclear Htt inclusions. The cytoplasmic Httex1 72Q inclusions appeared as highly organized inclusions that exhibit a dense core and a shell. Although previous studies have described Htt inclusions as being comprised of core and shell, these conclusions were based primarily on the preferential localization of other proteins in the periphery of mutant Htt inclusions in several cellular models[19,37,38,89] and transgenic mice[90]. These results were obtained using

immunofluorescence, however, the ultrastructural and biochemical properties of the core of the inclusions remained poorly defined. Our results show that cytoplasmic Htt inclusions are composed of highly organized fibrils in both the core and the periphery, although we cannot rule out the presence of entrapped oligomers in the core or at the surface close to the growing fibrils in the periphery[91]. These observations are consistent with a previous report by Qin *et al*. based on a FLAG-tagged Htt1-969 fragment (100Q), demonstrating that the Htt species in the core of the inclusions are highly protease-resistant and that oligomeric forms of Htt accumulate with cytoplasmic proteins and vesicles in the periphery of the inclusions[38].

The Nuclear Htt inclusions exhibited less complex ultrastructural properties, were less dense, and showed a more homogenous distribution of Htt aggregates throughout the inclusion. In contrast to cytoplasmic inclusions, no endomembranes or vesicles were detected in nuclear inclusions (Figure S6). These observations are consistent with most of the huntingtin nuclear inclusions found in HD mice models, which do not display the core and shell organization[23,28]. Our results suggest that the intracellular environment and interactions with lipids and endomembranes or vesicles are key determinants of the structural and molecular complexity of the inclusions and that different mechanisms drive the formation and maturation of the nuclear and cytosolic inclusions. Such differential characteristics between cytoplasmic and nuclear inclusions might account for the differential cellular dysfunction and toxicity associated with these two types of Htt inclusions[14,92–95].

Interestingly, the ultrastructural properties of the Httex1 cytoplasmic inclusions were strongly dependent on the length of the polyQ repeat[17] but not on the Nt17 domain (Figure 2). This is surprising given that *in vitro* and cellular studies have consistently shown that the Nt17 domain plays important roles in regulating the kinetics and structural properties of Htt aggregation[33] and Htt interactions with lipids and membranes[31,32,96–98]. Previous electron paramagnetic resonance (EPR) and solid-state nuclear magnetic resonance (solid-state NMR) studies of mutant Httex1 fibrils have proposed that mutant Httex1 form fibrils with a bottlebrush arrangement[99,100], with the polyQ domain making up the core of the fibrils[101], the Nt17 absorbed

to the polyQ, and the flexible proline-rich domain (PRD) exposed on the surface of the fibrils. In a recent study using ssNMR, Boatz *et al.* confirmed that the polyQ domain forms the core mutant Httex1 and showed that the Nt17 domain and part of the PRD (PPII helices) are buried to the core, while the other part of the PRD (random coil) is dynamic and accessible, and regulates multifilament assemblies *in vitro*[102]. Together, these observations could explain why the deletion of the Nt17 domain does not interfere with the organization of the inclusion and suggest that the interactions between the fibrils and other proteins and/or organelles are most likely mediated by the flexible PRD domain. Consistent with this model, removal of the PRD domain has been shown to 1) disrupt interactions with specific cellular proteins and Htt binding partners[103]; 2) inhibit the recruitment of dynamin, Htt interacting protein 1 (HIP1), and SH3-containing Grb2-like protein (SH3GL3) to the periphery of Htt inclusions in cells[38]; and 3) lead to a disorganization of the ultrastructural arrangement of the Htt inclusions[38].

We speculate that the formation of the core of the inclusions is guided predominantly by intermolecular interactions involving the polyQ domain and could be initiated by rapid events that are potentially driven by phase separation, as recently described by several groups[17,104–106]. The rapid formation of the aggregate's core does not allow for the regulated recruitment of other proteins and organelles (Figure 8A, 1-2), as evidenced by the fact that most antibodies against proteins found in Htt inclusion stain the periphery rather than the core of the inclusions[38]. The Nt17 most likely play key roles in the initial oligomerization events and, possibly, the packing or lateral association of the fibrils. Once this core of dense fibrils is formed, the fibrils at the periphery continue to grow through the recruitment of endogenous soluble proteins (Figure 8A, 3). Because this growth phase is slower, it allows the fibrils to interact with and/or recruit other proteins into the inclusions. Consistent with this hypothesis, Matsumoto and colleagues showed that the transcription factors TATA-binding protein (TBP) and CREB-binding protein (CBP)—containing a polyglutamine expansion—were present only at the periphery of the inclusions and not in the core[37]. Interestingly, although the length of the polyQ repeat did not seem to significantly influence the density of the fibrils at the core of the

inclusions, the peripheral organization of the Htt fibrils and the formation of the outer shell showed strong polyQ repeat length dependence (Figure 8A, 4). This model is supported by studies from Hazeki *et al.* and Kim *et al.,* demonstrating that the detergent-insoluble core of cellular Httex1 inclusions represents the skeletal structure of the inclusions, while the active surface dynamically interacts with Htt species and proteins being processed[47,107]. Altogether, our results highlight that the formation of Huntingtin inclusions occurs in two major phases with, first, the formation of the core driven primarily by the polyQ repeat domain, and then the growth of the inclusions with the addition of Htt fibrils and the recruitment of other proteins and organelles. The second phase appears to be driven by interactions involving both the polyQ and PRD domains and involves the active recruitment and sequestration of lipids, proteins, and membranous organelles (Figure 8A).

Proteome analysis points to a failure of the protein degradation machinery to clear Httex1 inclusions

Proteins from the UPS system[70] including ubiquitin moiety, E3 ubiquitin ligases (e.g., ITCH, RNF34, TRIM32, MARCH7), 26S proteasome subunits, and deubiquitinases formed the major cluster of the differentially enriched proteins in the Httex1 72Q inclusions. These results are in line with previous studies showing that Htt inclusions formed in HD patients or several cellular and *in vivo* models sequester several key components of the UPS system, including 26S proteasomes[108], deubiquitinases[109] (e.g., NEDD4 and USP5), and E3 ubiquitin ligases (e.g., ITCH, TRAF6, UBE3A, UHRF2, and Parkin) and induce impairment of the UPS[110–112]. In addition to components of the UPS system, proteins involved in autophagosome formation (optineurin[113]), maturation (ubiquilins[114]), and the process of autophagosome-lysosome fusion[115] (TOLLIP-interacting proteins and proteins involved in endolysosomal trafficking) were enriched inside the Httex1 72Q inclusions. Both TOLLIP[116–118] and optineurin[119–122] are critical for the efficient clearance of polyQ proteins aggregates[123] and in particular for the degradation of Htt aggregates. The depletion of TOLLIP in HeLa cells increases GFP-Htt-103Q-induced

toxicity[116] while optineurin knockdown promotes Htt aggregation. Finally, several chaperones from the Hsp70 and the DnaJ/HSp40 families, as well as ubiquilin-2, found previously enriched in Htt inclusions[47,124–126], were also sequestered inside the Httex1 72Q inclusions. Interestingly, it has recently been shown that the Hsp70 complex, together with the Hsp40/110 chaperone family, formed a disaggregase complex that can directly bind to Htt aggregates[127]. After disaggregation, Ubiquilin-2 interacts with Htt and shuttles the disaggregated species to the proteasome to promote its complete degradation[128]. The enrichment of the disaggregase chaperones network in the Httex1 72Q inclusions suggests that they were actively recruited but failed in their attempt to clear the Httex1 72Q aggregates. Together, these findings suggest that the cytosolic depletion of key proteins from the autophagolysosomal pathway, due to their sequestration inside the Httex1 pathological inclusions, could contribute to cellular dysfunction of the degradation and quality control machinery, as reported in HD human brain tissue[129].

The fusion of fluorescent proteins to mutant Httex1 significantly alters the biochemical and structural properties of mutant Htt

To enable the investigation of Htt aggregation dynamics using live imaging techniques, N-terminal Htt fragments are usually fused to large fluorescent proteins such as GFP[33,35,36,65,130,131]. To determine whether the fusion of these proteins to Httex1 significantly alters its aggregation properties and the final structure of Httex1 inclusions, we compared the biochemical, structural, and toxic properties of mutant Httex1 fused (or not) to GFP in our cellular model. To the best of our knowledge, this is the first study to directly compare inclusions formed by tag-free mutant native Httex1 proteins to GFP-tagged mutant Httex1 not only at the structural level by electron microscopy techniques but also at the biochemical level. Our results demonstrate that the fusion of the GFP tag to the Httex1 sequence significantly alters the proteome composition, structural organization and architecture of the Httex1 inclusions (Figures 1 and 6). The ultrastructure of Httex1 72Q-GFP inclusions revealed radiating fibrils with homogenous staining and the absence of the core and shell morphology.

In line with our findings, previous studies showed that cytoplasmic Httex1 72Q-GFP aggregates are fibrillar[17,132] and resemble other Httex1-GFP aggregates in COS cells[133], in primary striatal neurons[134] as well as aggregates formed by mutant Httex1 fused to a FLAG tag in HEK cells[18]. In a recent cryo-electron tomography (Cryo-ET) study, Bäuerlein *et al.* examined the ultrastructural properties of mutant Httex1 in the absence and presence of GFP and suggested that the presence of GFP does not significantly alter the organization of the cytoplasmic inclusions in HeLa and neurons[15]. Similar to our findings, they showed that the presence of the GFP tag 1) induces a 50% reduction in fibril density and a 25% increase in fibril stiffness; 2) results in increased spacing between the fibrils in the Httex1-GFP inclusions; and; 3) does not influence the overall size of the inclusions.

However, when it comes to the ultrastructural properties of the tag-free mutant Httex1 inclusions, we observed very different results. In our studies, the inclusions formed by the tag-free mutant Httex1 exhibited the core and shell structure, which was not observed for any of the inclusions studied by Bäuerlein *et al.* Careful examination of the sequence of the constructs they used reveals a Myc-tag at the N-terminal side of their Httex1 proteins, whereas the constructs we used contain only the native sequence of mutant Httex1. While we showed that removal of the Nt17 domain does not influence the ability of tag-free Htt to form inclusions with the core and shell organization, the fusion of additional amino acids in the N-terminus could still significantly alter the kinetics, oligomerization, and aggregation pathway of Httex1 protein. In addition to differences at the ultrastructural levels, our studies showed the recruitment of membranous organelles and vesicles as disrupted structures inside the inclusions in both the core and shell but also in the form of intact ER-mitochondrial network at the periphery of the tag-free inclusions. Less internalized structures were observed in the Httex1-GFP inclusions, consistent with the findings of Bäuerlein *et al.*[15]. Another major difference between the two studies is that Bäuerlein *et al.* did not observe any polyQ-length effect on the size or ultrastructural properties of the inclusions formed by mutant Httex1-GFP over the polyQ repeat range of 64Q to 97Q. Although the presence of GFP can explain the differences between the two results, it is also possible that these differences could also be because the authors

compared polyQ repeats that are far beyond the pathogenic threshold. We believe that in this polyQ range, the difference in aggregation properties between 64 and 97Q would be small compared to what one would observe when comparing mutant Httex1 with polyQ repeats close to the pathogenic threshold (39-43Q). Therefore, in our study, we compared the ultrastructure properties of the inclusions of Httex1 containing 39 or 72Q repeats. In our experiments, the inclusions formed by mutant Httex1 39Q were found to be less organized and did not exhibit a stable core and shell arrangement as in the case of Httex1 72Q.

To date, no study has compared the protein content of Htt inclusions formed in the presence or absence of a fluorescent of solubilizing tag. To address this gap, we have compared the proteome of Httex1 72Q inclusions in the presence or absence of the GFP tag. Our results show that although the top two biological processes enriched in the Httex1 inclusions were similar, namely, the protein quality control machinery (UPS system, autophagy pathway, and the chaperones network), and the transcriptional-related pathways, the degree of enrichment of proteins as well as the class of proteins enriched was different in both types of inclusions. Approximately 50% of the proteome of the tag-free inclusions were related to proteins involved in transcriptional pathways, while in the inclusions formed by Httex1 72Q-GFP, this biological process represents ~14%. Transcriptional dysregulation[135,136] is one of the major features of HD and occurs at the onset of the early neuropathological symptoms in HD patients. Several proteins related to gene expression, the chromatin remodeling and histone acetylation process[137] (SETD2[138,139]), transcription initiation (TFIID subunit[140]), regulation (NF-Y[141]) and elongation (TCERG1[142]) factors, TATA-box binding proteins (TBP[124,143]) that have been shown to either lose their function in HD through their interaction with Htt and/or sequestration in the *bona fide* Htt inclusions[139,142] were specifically enriched in the tag-free inclusions but not in the GFP-Httex1 72Q inclusions. Similarly, although biological processes related to autophagy were found to be enriched, in both types of inclusions, ~33% of the identified proteins were different in the GFP-Httex1 72Q inclusions. For example, optineurin—an autophagy receptor implicated in HD pathology—was sequestered in the inclusions formed by the tag-free

inclusions and the *bona fide* Htt inclusions in the HD brain[4] but not in the GFP-Httex1 72Q inclusions. Instead, CHMP2b was specifically enriched in the GFP-Httex1 72Q inclusions. CHMP2b, together with several proteins from the ESCRT complexes, is known as the ESCRTing autophagic complex involved in the clearance of specific aggregating proteins[144]. This suggests that selective autophagy pathways are engaged in response to different types of aggregates.

Proteins related to infection and inflammation pathways, including the TNF, the Toll-like receptor, and the NOD-like receptor signaling pathways, were only sequestered in the tag-free inclusion. This is particularly relevant because neuroinflammation has been implicated in HD pathology[145]. On the other hand, a significant number of metabolic-proteins were exclusively enriched in the GFP-like inclusions. Therefore, despite the similarities in terms of general pathways impacted, the cellular responses or the mechanisms underlying cellular dysfunctions and toxicity are specific to the type of inclusions formed in the cells. Our results also strengthen the idea that inclusions formed from GFP-Httex1 72Q do not exhibit the same behavior as the tag-free inclusion.

Tag-free and GFP Httex1 inclusions differentially impact mitochondrial and ER-related functions in the cells

Mitochondrial fragmentation[146] and inflammation[147] are hallmarks of Htt-induced neurodegeneration. Interestingly, only tag-free Httex1 72Q overexpression results in mitochondrial fragmentation and is characterized by the strong accumulation of inflammation-linked proteins in the aggregates. We speculate that the observed hyper-activation of mitochondrial respiration (in the absence of significantly increased ROS production) is an adaptation of the inclusion-bearing cells in order to generate sufficient energy by oxidative phosphorylation for increased energetic demands for unfolding or clearance of aggregating proteins. We also demonstrated modulation of ERES with the presence of GFP at the C-terminal part of Httex1 72Q; the effect is reduced compared to tag-free Httex1 inclusions but

still indicates ER perturbation consistent with the previous cryo-ET report[15], suggesting decreased ER dynamics near Httex1-GFP inclusions.

Overall, we demonstrated drastic differences in the architecture, composition, and impact on cellular organelles by the inclusions formed by Httex1 72Q in the absence and presence of GFP (Figure 8B and Figure S23). Altogether, our data suggest that the aggregation processes of unmodified and GFP-tagged Httex1 are distinct, thus underscoring the potential limitations of using GFP to investigate the molecular, biochemical, and cellular determinants of Htt aggregation and mechanisms of toxicity.

Conclusion

In summary, our integrative imaging and proteomic studies demonstrate that the process of Htt cytoplasmic inclusion formation occurs in at least two phases and involves the active recruitment of lipids, proteins, and organelles. The organization and ultrastructure properties of these inclusions are greatly influenced by the polyQ repeat length and the intracellular environment, as evidenced by the fact that cytoplasmic and nuclear Httex1 inclusions exhibit distinct ultrastructural properties.

The specific core and shell organization of tag-free Httex1 72Q inclusions suggests that the periphery plays an important role in the maturation of the inclusion and potentially Htt-mediated toxicity. We demonstrated that the Nt17 domain is not required for the final structural arrangement of the inclusion and showed that the polyQ and the PRD play a dominant role in mediating Htt inclusion formation and interactions with proteins and organelles at the periphery of the inclusions, respectively.

Finally, we showed that GFP-tagged proteins could still represent useful tools for investigating the mechanisms and modulators of Htt fibril formation in cells, but underscored the critical importance of using tag-free native Htt sequences to investigate the mechanisms of inclusion formation and maturation and Htt toxicity. Taken together, we believe that extending the studies and approaches presented here to other HD model systems will pave the way to a

better understanding of the mechanisms of Htt inclusion formation and how it contributes to the development of HD. This will also enable the more effective use of these models to assess the therapeutic potential of targeting different stages of Htt inclusion formation and maturation.

Materials & Methods

DNA constructs and purification

pCMV mammalian expression vector encoding for Httex1 16Q, Httex1 16Q-GFP, Httex1 39Q, Httex1 39Q-GFP, Httex1 72Q, and Httex1 72Q-GFP were kindly provided by Andrea Caricasole (IRBM). ΔN17-Httex1 39Q, ΔN17-Httex1 39Q-GFP, ΔN17-Httex1 72Q, and ΔN17-Httex1 72Q-GFP were purchased from GeneArt (Germany). Plasmids were transformed into Chemo-competent E. coli stable 3 cells (Stbl3) from Life Technologies (Switzerland), and Maxiprep plasmid purification (Life Technologies, Switzerland) was performed following the manufacturer's instructions.

Cell culture and plasmid transfection

HEK 293 cells were maintained in Dulbecco's modified Eagle's medium DMEM (Life Technologies, Switzerland) containing 10% FBS (Life Technologies, Switzerland), 10 µg/ml streptomycin and penicillin (Life Technologies, Switzerland) in a humidified incubator, and 5% CO_2 at 37°C. Cells were plated at a density of 100,000 per dish in glass-bottom µ-Dishes (IBIDI) or 50,000 cells/well in 24 well plates with a Thermanox Plastic Coverslip (round) 13mm in diameter (Life Technologies, Switzerland) in order to obtain cells at a 70-90% confluence the day after for the transfection procedure using a standard calcium phosphate procedure[160]. Briefly, 2µg of DNA was diluted in 30µl H2O and 30µl of 0.5M CaCl2 before the dropwise addition of 60µl of 2xHBS, pH 7.2 (50mM HEPES, pH 7.05; 10mM KCL; 12mM dextrose; 280mM NaCl; 1.5mM Na2PO4, pH 7.2 dissolved in H2O) under mild vortexing condition.

Immunocytochemistry (ICC)

Forty-eight hours after transfection, HEK 293 cells were washed twice with PBS pH 7.4 (1X) (Life Technologies, Switzerland) and fixed in 3.7% formaldehyde (Sigma-Aldrich, Switzerland) in PBS (PFA) for 15 min at room temperature (RT). After a blocking step with 3% BSA (Sigma-

Aldrich, Switzerland) diluted in 0.1% Triton X-100 (Applichem, Germany) in PBS (PBST) for 30 min at RT, cells were incubated with the primary antibodies (Figure S1) anti-htt raised against the Nt17 domain (2B7, CHDI [Cure Huntington's Disease Initiative]; Ab109115, Abcam) or the PolyQ (MW1, CHDI) or Proline-Rich Domain (PRD) (MAB5492, Millipore; 4C9, CHDI; N18, Santa-Cruz and EGT 414), or against Htt (S830) at a dilution of 1/500 in PBST for 2h at RT. Cells were then rinsed five times in PBST and incubated for 1h at RT with the secondary donkey anti-mouse Alexa647, donkey anti-rabbit Alexa647, or donkey anti-goat 568 antibodies (Life Technologies, Switzerland) used at a dilution of 1/800 in PBST. Phalloidin Atto594 (Sigma-Aldrich, Switzerland), a specific fluorescent label against F-actin, was used at a dilution of 1/50 and DAPI (Sigma-Aldrich, Switzerland) at 2µg/ml, all diluted in PBST. Cells were then washed five times in PBST, and a last one in double-distilled H2O, before being mounted in polyvinyl alcohol (PVA) mounting medium with DABCO (Sigma-Aldrich, Switzerland). Cells were examined with a confocal laser-scanning microscope (LSM 700, Zeiss, Germany) with a 40x objective and analyzed using Zen software (Zeiss, Germany).

Immunofluorescence staining of ER exit sites

A total of 100,000 HeLa cells were seeded into a 6-well plate on glass coverslips. After 24 h, cells were transfected with the different variants of GFP-tagged or tag-free Httex1 using Fugene 6 according to the manufacturer's instructions. An empty vector was used as a negative control. Forty-eight hours after transfection, cells were fixed in 4% PFA for 20 min and stained using an anti-Htt antibody (Millipore, mouse monoclonal (MAB5492)). Briefly, after cells were washed with PBS containing 20 mM glycine, slides were incubated in a blocking buffer composed of 3% BSA (Bovine Serum Albumin) in 0.1% Triton X-100 and PBS for 30 min at RT. Subsequently, cells were incubated with the primary antibodies against Htt and Sec13 (R&D Systems) to label ER exit sites, followed by washing and incubation with Alexa-Fluor tagged secondary antibodies. Slides were washed with PBS and embedded in polyvinyl

alcohol mounting medium with DABCO (Sigma-Aldrich). Cells were imaged with 63x objective using a Zeiss LSM 700 confocal microscope.

In the case of Httex1-FP, cells were washed in PBS containing 20mM glycine followed by permeabilization in PBS containing 0.2% Triton X-100. Subsequently, cells were incubated with primary antibody to stain ER exit sites diluted in 3% BSA in PBS. After being washed with PBS, cells were incubated with the appropriate Alexa-Fluor tagged secondary antibodies in 3% BSA-PBS. Slides were washed with PBS and embedded in polyvinyl alcohol mounting medium with DABCO (Sigma-Aldrich). Cells were imaged with 63x objective using a Zeiss LSM 700 confocal microscope

Quantification of ER exit sites' number and size was performed using the analyze particles tool in Image J after thresholding for pixel size and intensity.

Correlative light and electron microscopy (CLEM)

HEK 293 cells were grown at 600,000 cells/ml on 35 mm dishes with alphanumeric searching grids etched on the bottom glass (MatTek Corporation, Ashland, MA, USA). Forty-eight hours after transfection with either Empty vector (EV), Httex1 72Q, or Httex1 72Q-GFP, cells were fixed for 2h with 1% glutaraldehyde (Electron Microscopy Sciences, USA) and 2.0% PFA in 0.1 M phosphate buffer (PB) at pH 7.4. After washing with PBS, ICC was performed as described above. Intra-cellular inclusions were stained with an Htt antibody (Millipore MAB5492, aa 1-82) and the cells of interest were imaged with a fluorescence confocal microscope (LSM700, Carl Zeiss Microscopy) with a 40x objective. The precise position of the selected cells was recorded using the alpha-numeric grid etched on the dish bottom. The cells were then fixed further with 2.5% glutaraldehyde and 2.0% PFA in 0.1 M PB at pH 7.4 for another 2h. After 5 washings of 5 min with 0.1 M cacodylate buffer at pH 7.4, cells were post-fixed with 1% osmium tetroxide in the same buffer for 1h and then washed with double-distilled water before contrasted with 1% uranyl acetate water for 1h. The cells were then dehydrated in increasing concentrations of alcohol (2 × 50%, 1 × 70%, 1 × 90%, 1 × 95%, and 2 × 100%)

for 3 min each wash. Dehydrated cells were infiltrated with Durcupan resin (Electron Microscopy Sciences, Hatfield, PA, USA) diluted with absolute ethanol at 1: 2 for 30 min, at 1: 1 for 30 min, at 2: 1 for 30 min, and twice with pure Durcupan for 30 min each. After 2h of incubation in fresh Durcupan resin, the dishes were transferred into a 65°C oven so that the resin could polymerize overnight. Once the resin had hardened, the glass CS on the bottom of the dish was removed by repeated immersion in hot water (60°C), followed by liquid nitrogen. The cell of interest was then located using the previously recorded alphanumeric coordinates, and a razor blade was used to cut this region away from the rest of the resin. This piece was then glued to a resin block with acrylic glue and trimmed with a glass knife using an ultramicrotome (Leica Ultracut UCT, Leica Microsystems). Next, ultrathin sections (50–60 nm) were cut serially from the face with a diamond knife (Diatome, Biel, Switzerland) and collected on 2 mm single-slot copper grids coated with formvar plastic support film. Sections were contrasted with uranyl acetate and lead citrate and imaged with a transmission electron microscope (Tecnai Spirit EM, FEI, The Netherlands) operating at 80 kV acceleration voltage and equipped with a digital camera (FEI Eagle, FEI).

Sample processing for electron microscopy imaging without cell permeabilization

Forty-eight hours after transfection, HEK 293 cells were fixed in PFA 2% and glutaraldehyde 2% in phosphate buffer 0.1M (pH 7.4) for 1h and 30 min. To preserve the internal membranes of the cells, no ICC was performed. Cells were then washed 3 times for 5 min in cacodylate buffer (0.1M, pH 7.4). Next, they were post-fixed with 1% osmium tetroxide plus 1.5% potassium ferrocyanide in cacodylate buffer (0.1M, pH 7.4) at RT for 40min, followed by post-fixation with 1% osmium tetroxide in cacodylate buffer (0.1M, pH 7.4) at RT for 40min. Samples were washed twice for 5 min in distilled water, then further stained in 1% uranyl acetate in water for 40 min and washed once in double-distilled water for 5min. The samples were dehydrated in increasing concentrations of ethanol for 3 min each wash (2X50%, 1X70%, 1X90%, 1X95%, 2X100%) and then embedded in epoxy resin (Epon had the formula: Embed 812: 20g, DDSA: 6.1g, NMA: 13.8g, DMP 30: 0.6g) (Electron Microscopy Sciences, USA)

through the continuous rotation of vials. The embedding process starts with a 1:1 ethanol:epon mix for 30min, followed by 100% EPON for 1h. EPON was then replaced with fresh EPON for 2h. Finally, samples were embedded between coated glass slides and placed in an oven at 65°C overnight. 50nm thick serial sections were cut with an ultramicrotome (UC7, Leica Microsystems, Germany) and collected on formvar support films on single-slot copper grids (Electron Microscopy Sciences, USA) for transmission electron microscopy imaging (TEM). TEM images were taken at 80 kV filament tension with a Tecnai Spirit EM microscope, using an Eagle 4k x 4k camera. At least 8 cells were imaged per condition at 2900x and 4800x magnification.

Images were aligned using Photoshop software (Adobe, USA) and different organelles (Nucleus, Mitochondria, Endoplasmic Reticulum, Httex1 inclusions) were first segmented manually using the arealist function in the trackEM2 plugin in the FIJI software. We then moved to a custom-developed machine learning-based pipeline, tailored specifically to 3D microscopy data (www.ariadne-service.ch) after validation using the manual segmentation for reference. At the end of the segmentation process, the different segmented areas were exported as serial image masks, then visualized as objects in the 3D viewer plugin in FIJI and exported as wavefront in the Blender® 3D modeling software (Blender Foundation). Using Blender®, the 3D axes were first corrected according to the model orientation and the Z scale was adjusted. Httex1 inclusion, mitochondria, and the nucleus were smoothed and the Httex1 inclusion was adjusted to visualize intra-aggregates membranous structures within the inclusion.

Preparation of protein samples for biochemical analyses

Samples were generated, in duplicate, of the HRR experiment for analysis of mitochondrial markers by WB and FT. Transfected cells were lysed in 75µl of RIPA buffer (150Mm NaCl, 1µ NP40, 0.5% Déoxycholate, 0.1% Sodium dodecyl sulfate (SDS), 50Mm Tris pH 8). Cell lysates were incubated at 4°C for 20 min and then cleared by centrifugation at 4°C for 20 min at 16 000g. Supernatants were collected as soluble protein fraction and stored at -20°C after LB5x addition and 5 min of boiling. BCA was performed on the RIPA soluble fraction. Pellets were

washed with 500ul of PBS, then centrifuged again for 5 min at 16,000g. Supernatants were discarded and the pellet resuspended in 30µl of PBS supplemented with SDS 2% and sonicated with a fine probe [3 times, 3 sec at the amplitude of 60% (Sonic Vibra Cell, Blanc Labo, Switzerland)]. Cellulose acetate membrane was first equilibrated with 2% SDS (in PBS) for 5 min and the filter main fold arranged on top of 2 Watman papers inside the Bio-Dot Apparatus (#1706545, USA). Samples were loaded and filtered by vacuum. The membrane was washed 3 times by 0.5% SDS in PBS and applying the vacuum. The acetate membrane was then removed and washed once in PBS-Tween 1%. WB and FT membranes were blocked overnight with Odyssey blocking buffer (LiCor) and then incubated at RT for 2h with different primary antibodies (anti-huntingtin MAB5492 and anti-VDAC1) diluted in the same blocking buffer (1/5000). Membranes were washed in PBS-Tween 1% and then incubated with secondary antibody diluted in blocking buffer (1/5000) for 1h at RT before a final wash in PBS-Tween 1%. The protein detection was performed by fluorescence using Odyssey CLx from LiCor. The signal intensity was quantified using Image Studio 3.1 from LiCor.

Preparation of samples for mass spectrometry

Samples were generated in triplicate for quantitative mass spectrometry analysis. Forty-eight hours post-transfection, cells were lysed in PBS supplemented by 0.5% NP40, 0.5% Triton x100, 1% protease cocktail inhibitor (Sigma PB340), and 1% Phenylmethanesulfonyl Fluoride (PMSF, Applichem). Cell lysates were incubated at 4°C for 20 min and then cleared by centrifugation at 4°C for 20 min at 20,000g. Supernatants were collected as non-ionic soluble protein fraction. Pellets were washed and resuspended in PBS supplemented by 2% N-Lauroylsarcosine sodium salt (Sarkosyl, Sigma) with protease inhibitors. The pellets were briefly sonicated with a fine probe [3 times, 3 sec at the amplitude of 60% (Sonic Vibra Cell, Blanc Labo, Switzerland)], incubated 5 min on ice, then centrifuged at 100,000g for 30 min at 4°C. Supernatants were collected as Sarkosyl soluble fraction. Pellets were washed with the previous buffer and resuspended in PBS supplemented by 2% Sarkosyl and 8M Urea and

briefly sonicated as done previously. Laemli Buffer 4x was added to samples and then samples were boiled at 95°C. Samples were separated by SDS-PAGE on a 16% polyacrylamide gel, for Coomassie staining and WB.

For WB, nitrocellulose membranes were blocked overnight with Odyssey blocking buffer (LiCor) and then incubated at RT for 2h with Htt primary antibodies (MAB5492) diluted in PBS (1/5000). Membranes were washed in PBS-Tween 1% and then incubated with secondary antibody diluted in PBS (1/5000) for 1h at RT before a final wash in PBS-Tween 1%. The protein detection was performed by fluorescence using Odyssey CLx from LiCor. The signal intensity was quantified using Image Studio 3.1 from LiCor.

For proteomic identification, the samples separated by SDS-PAGE were then stained with Coomassie blue. Each gel lane was entirely sliced and proteins were In-gel digested as previously described[149]. Peptides were desalted on stagetips[150] and dried under a vacuum concentrator. For LC-MS/MS analysis, resuspended peptides were separated by reversed-phase chromatography on a Dionex Ultimate 3000 RSLC nano UPLC system connected in-line with an Orbitrap Lumos (Thermo Fisher Scientific, Waltham, USA). Protein identification and quantification were performed with the search engine MaxQuant 1.6.2.10[151]. The Human Uniprot database (last modified: 2019-06-11, 74468 canonical and isoform sequences + Httex1 Sequence) was used. Carbamidomethylation was set as a fixed modification, whereas oxidation (M), phosphorylation (S, T, Y), acetylation (Protein N-term), and glutamine to pyroglutamate were considered as variable modifications. A maximum of two missed cleavages was allowed. “Match between runs” was enabled. A minimum of 2 peptides was allowed for protein identification and the false discovery rate (FDR) cut-off was set at 0.01 for both peptides and proteins. Label-free quantification and normalization were performed by Maxquant using the MaxLFQ algorithm, with the standard settings[152]. In Perseus[153], reverse proteins, contaminants, and proteins identified only by sites were filtered out. Data from the Urea fraction were analyzed separately following the same workflow. Biological replicates were grouped together and protein groups containing a minimum of two LFQ values in at least one

group were conserved. Missing values were imputed with random numbers using a gaussian distribution (width = 0.7, down-shift = 1.9 for Urea fraction). Differentially expressed proteins were highlighted by a two-sample t-test, followed by a permutation-based correction (False Discovery Rate). Significant hits were determined by a volcano plot-based strategy, combining t-test P-values with ratio information[154]. Significance curves in the volcano plot corresponded to a S0 value of 0.5 and a FDR cut-off of 0.05. Further graphical displays were generated using homemade programs written in R (version 3.6.1)[155].

Respirometry and amplex red fluorometry

Wild-type HEK 293 cells were transfected 24h after plating with Htt 16Q, Htt 72Q, Htt 16Q-GFP, or Htt 72Q-GFP. Forty-eight hours after transfection, cells were gently detached using 0.05% trypsin, resuspended in DMEM, counted, and immediately used for high-resolution respirometry.

One million cells were transferred to MiR05 (0.5 mM EGTA, 3mM $MgCl_2$, 60 mM potassium lactobionate, 20 mM taurine, 10 mM KH_2PO_4, 20 mM HEPES, 110 mM sucrose, and 0.1% (w/v) BSA, pH=7.1) in a calibrated, 2ml high-resolution respirometry oxygraph chamber (Oroboros Instruments, Austria) kept stably at 37°C. Mitochondrial ROS production (O_2^- and H_2O_2) was measured using amplex red fluorometry and O2K Fluo-LED2 modules (Oroboros Instruments, Austria) as described previously[156]. Briefly, for amplex red fluorometry, cells were added to oxygraph chambers after the addition of 10 µM amplex red, 1 U/ml horseradish peroxidase, and 5 U/ml superoxide dismutase to MiR05 and calibration with known H_2O_2 concentrations. Fluorescence was measured during the subsequently applied high-resolution respirometry protocol.

Routine respiration (and mitochondrial ROS production) was measured from intact cells, after which plasma membranes were permeabilized by the application of an optimized (integrity of

mitochondrial outer membranes verified by the cytochrome c test) concentration of digitonin (5 µg/mL).

Oxygen flux at different respirational states on permeabilized cells was then determined using the substrate-uncoupler-inhibitor-titration (SUIT) protocol as described previously[157,158]. Briefly, NADH-pathway (N) respiration in the LEAK and oxidative phosphorylation (OXPHOS) state was analyzed in the presence of malate (2mM), pyruvate (10mM), and glutamate (20mM) before and after the addition of ADP (5 mM), respectively (N_L, N_P). The addition of succinate (10 mM) allowed for the assessment of NADH- and succinate-linked respiration in OXPHOS (NS_P) and in the uncoupled state (NS_E) after the incremental (Δ0.5 µM) addition of carbonyl cyanide m-chlorophenyl hydrazine (CCCP). The inhibition of Complex I by rotenone (0.5 µM) yielded succinate-linked respiration in the uncoupled state (S_E). Tissue-mass specific oxygen fluxes were corrected for residual oxygen consumption, *Rox*, measured after additional inhibition of the mitochondrial electron transport system, ETS, Complex III with antimycin A. For further normalization, fluxes of all respiratory states were divided by ET-capacity to obtain flux control ratios, FCR. Terminology was applied according to http://www.mitoeagle.org/index.php/MitoEAGLE_preprint_2018-02-08.

Mitochondrial ROS values were corrected for background fluorescence and respirational states before the addition of the uncoupler used for analysis.

Statistical Analysis

All the experiments have been independently repeated a minimum of three times. The statistical analyses were performed using Student's *t*-test or ANOVA test followed by a Tukey-Kramer *post-hoc* test using KaleidaGraph (RRID:SCR_014980). The data were regarded as statistically significant at $p<0.05$.

References

1. Cattaneo E, Rigamonti D, Goffredo D, Zuccato C, Sipione S, Cattaneo E. Loss of normal huntingtin function : new developments in Huntington ' s disease research. *TRENDS Neurosci*. 2001;24(3):182-188.
2. Ross C a, Aylward EH, Wild EJ, et al. Huntington disease: natural history, biomarkers and prospects for therapeutics. *Nat Rev Neurol*. 2014;10(4):204-216.
3. Stout JC, Paulsen JS, Queller S, et al. Neurocognitive Signs in Prodromal Huntington Disease. *Neuropsychology*. 2012;25(1):1-14.
4. Macdonald ME, Ambrose CM, Duyao MP, et al. A Novel Gene Containing a Trinucleotide That Is Expanded and Unstable on Huntington ' s Disease Chromosomes. *Cell*. 1993;72:971-983.
5. Kremer B, Goldberg P, Andrew SE, et al. A worldwide study of the huntington's disease mutation. *N Engl J Med*. 1994;330.
6. Lee J, Ramos EM, Lee J, Gillis T. CAG repeat expansion in Huntington disease determines age at onset in a fully dominant fashion. *Neurology*. 2012.
7. Lee JM, Correia K, Loupe J, et al. CAG Repeat Not Polyglutamine Length Determines Timing of Huntington's Disease Onset. *Cell*. 2019;178(4):887-900.e14.
8. Steffan JS, Agrawal N, Pallos J, et al. SUMO modification of Huntingtin and Huntington's disease pathology. *Science*. 2004;304(5667):100-104.
9. Rockabrand E, Slepko N, Pantalone A, et al. The first 17 amino acids of Huntingtin modulate its sub-cellular localization, aggregation and effects on calcium homeostasis. *Hum Mol Genet*. 2007;16(1):61-77.
10. Tam S, Spiess C, Auyeung W, et al. The chaperonin TRiC blocks a huntingtin sequence element that promotes the conformational switch to aggregation. *Nat Struct Mol Biol*. 2009;16(12):1279-1285.
11. Thakur AK, Jayaraman M, Mishra R, et al. Polyglutamine disruption of the huntingtin exon1 N-terminus triggers a complex aggregation mechanism Ashwani. *Nat Struct Mol Biol*. 2009;16(4):380-389.
12. Thompson LM, Aiken CT, Kaltenbach LS, et al. IKK phosphorylates Huntingtin and targets it for degradation by the proteasome and lysosome. *J Cell Biol*. 2009;187(7):1083-1099.
13. Gu X, Greiner ER, Mishra R, et al. Serines 13 and 16 Are Critical Determinants of Full-length Human Mutant Huntingtin-Induced Disease Pathogenesis in HD Mice. *Neuron*. 2009;64(6):828-840. doi:10.1016/j.neuron.2009.11.020.
14. Zheng Z, Li A, Holmes BB, Marasa JC, Diamond MI. An N-terminal nuclear export signal regulates trafficking and aggregation of huntingtin (Htt) protein exon 1. *J Biol Chem*. 2013;288(9):6063-6071.
15. Bäuerlein FJB, Saha I, Mishra A, et al. In Situ Architecture and Cellular Interactions of PolyQ Inclusions. *Cell*. 2017;171(1):179-187.e10.
16. Gruber A, Hornburg D, Antonin M, et al. Molecular and structural architecture of polyQ aggregates in yeast. *Proc Natl Acad Sci*. 2018;115(15):201717978.
17. Peskett TR, Rau F, O'Driscoll J, Patani R, Lowe AR, Saibil HR. A Liquid to Solid Phase Transition Underlying Pathological Huntingtin Exon1 Aggregation. *Mol Cell*. 2018:1-14.
18. Waelter S, Boeddrich A, Lurz R, et al. Accumulation of mutant huntingtin fragments in aggresome-like inclusion bodies as a result of insufficient protein degradation. *Mol Biol Cell*. 2001;12(5):1393-1407.
19. Tagawa K, Hoshino M, Okuda T, et al. Distinct aggregation and cell death patterns among different types of primary neurons induced by mutant huntingtin protein. *J Neurochem*. 2004;89(4):974-987.
20. Wellington CL, Ellerby LM, Gutekunst C-A, et al. Caspase cleavage of mutant huntingtin precedes neurodegeneration in Huntington's disease. *J Cell Biol*. 2002;22(4):749-759.
21. Neueder A, Landles C, Ghosh R, et al. The pathogenic exon 1 HTT protein is

produced by incomplete splicing in Huntington's disease patients. *Sci Rep*. 2017;7(1):1307.
22. Schilling G, Klevytska A, Tebbenkamp ATN, et al. Characterization of huntingtin pathologic fragments in human Huntington disease, transgenic mice, and cell models. *J Neuropathol Exp Neurol*. 2007;66(4):313-320.
23. Davies SW, Turmaine M, Scherzinger E, Wanker EE, Mangiarini L, Bates GP. Formation of Neuronal Intranuclear Inclusions Underlies the Neurological Dysfunction in Mice Transgenic for the HD Mutation. *Cell*. 1997;90:537-548.
24. Mangiarini L, Sathasivam K, Seller M, et al. Exon I of the HD gene with an expanded CAG repeat is sufficient to cause a progressive neurological phenotype in transgenic mice. *Cell*. 1996;87(3):493-506.
25. Diane Martindale, Abigail Hackam, Andrew Wieczorek, Lisa Ellerby, Cheryl Wellington, Krista McCutcheon, Roshni Singaraja, Parsa Kazemi-Esfarjani, Richard Devon, Seung U. Kim, Dale E. Bredesen, Frank Tufaro & MRH. Length of huntingtin and its polyglutamine tract influences localization and frequency of intracellular aggregates. *Nat Genet*. 1998;18(3):231-236.
26. Barbaro BA, Lukacsovich T, Agrawal N, et al. Comparative study of naturally occurring Huntingtin fragments in Drosophila points to exon 1 as the most pathogenic species in Huntington's disease. *Hum Mol Genet*. 2015;24(4):913-925.
27. Scherzinger E, Sittler A, Schweiger K, et al. Self-assembly of polyglutamine-containing huntingtin fragments into amyloid-like fibrils: implications for Huntington's disease pathology. *Proc Natl Acad Sci U S A*. 1999;96(8):4604-4609.
28. Scherzinger E, Lurz R, Turmaine M, et al. Huntingtin encoded polyglutamine expansions form amyloid-like protein aggregates in vitro and in vivo. *Cell*. 1997;90:549-558.
29. Hollenbach B, Scherzinger E, Schweiger K, Lurz R, Lehrach H, Wanker EE. Aggregation of truncated GST--HD exon 1 fusion proteins containing normal range and expanded glutamine repeats. *Philos Trans R Soc B Biol Sci*. 1999;354(1386):991-994.
30. Ansaloni A, Wang ZM, Jeong JS, Ruggeri FS, Dietler G, Lashuel HA. One-pot semisynthesis of exon 1 of the Huntingtin protein: New tools for elucidating the role of posttranslational modifications in the pathogenesis of Huntington's disease. *Angew Chemie - Int Ed*. 2014;53(7):1928-1933.
31. James R. Arndta, Maxmore Chaibvaa, and Justin Legleitera, b, c At. The emerging role of the first 17 amino acids of huntingtin in Huntington's disease. *Biomol Concepts*. 2016;8(5):583-592.
32. Atwal RS, Xia J, Pinchev D, Taylor J, Epand RM, Truant R. Huntingtin has a membrane association signal that can modulate huntingtin aggregation, nuclear entry and toxicity. *Hum Mol Genet*. 2007;16(21):2600-2615.
33. Shen K, Calamini B, Fauerbach JA, et al. Control of the structural landscape and neuronal proteotoxicity of mutant Huntingtin by domains flanking the polyQ tract. *Elife*. 2016;5:1-29.
34. Maiuri T, Woloshansky T, Xia J, Truant R. The huntingtin N17 domain is a multifunctional CRM1 and ran-dependent nuclear and cilial export signal. *Hum Mol Genet*. 2013;22(7):1383-1394.
35. Iwata A, Riley BE, Johnston JA, Kopito RR. HDAC6 and microtubules are required for autophagic degradation of aggregated Huntingtin. *J Biol Chem*. 2005;280(48):40282-40292.
36. Mantha N, Das NG, Das SK. Recent Trends in Detection of Huntingtin and Preclinical Models of Huntington ' s Disease. *Hindawi Publ*. 2014;2014.
37. Matsumoto G, Kim S, Morimoto RI. Huntingtin and mutant SOD1 form aggregate structures with distinct molecular properties in human cells. *J Biol Chem*. 2006;281(7):4477-4485.
38. Qin Z, Wang Y, Sapp E, et al. Huntingtin Bodies Sequester Vesicle-Associated Proteins by a Polyproline-Dependent Interaction. *J Neurosci*. 2004;24(1):269-281.

39. Panov A V, Gutekunst C, Leavitt BR, et al. Early mitochondrial calcium defects in Huntington ' s disease are a direct effect of polyglutamines. *Nat Neurosci*. 2002:731-736.
40. Costa V, Scorrano L. Shaping the role of mitochondria in the pathogenesis of Huntington ' s disease. *EMBO J*. 2012;31(8):1853-1864.
41. Ghosh R, Wood-Kaczmar A, Dobson L, et al. Expression of mutant exon 1 huntingtin fragments in human neural stem cells and neurons causes inclusion formation and mitochondrial dysfunction. *FASEB J*. 2020;(March):1-16.
42. Hackam AS, Hodgson JG, Singaraja R, et al. Huntington ' s Disease in Cell Culture and in Transgenic Mice Expressing Mutant Huntingtin Evidence for both the nucleus and cytoplasm as subcellular sites of pathogenesis in Huntington ' s disease in cell culture and in transgenic mice expressing mutant. *Philos Trans R Soc B Biol Sci*. 2019;354(1386).
43. Sapp E, Schwarz C, Chase K, et al. Huntingtin localization in brains of normal and Huntington's disease patients. *Ann Neurol*. 1997;42(4):604-612.
44. DiFiglia M, Sapp E, Chase K, et al. Huntingtin is a cytoplasmic protein associated with vesicles in human and rat brain neurons. *Neuron*. 1995;14(5):1075-1081.
45. Sahoo B, Singer D, Kodali R, Zuchner T, Wetzel R. Aggregation behavior of chemically synthesized, full-length huntingtin exon1. *Biochemistry*. 2014;53(24):3897-3907.
46. Vieweg S, Ansaloni A, Wang ZM, Warner JB, Lashuel HA. An intein-based strategy for the production of tag-free huntingtin exon 1 proteins enables new insights into the polyglutamine dependence of Httex1 aggregation and fibril formation. *J Biol Chem*. 2016;291(23):12074-12086.
47. Kim YE, Hosp F, Frottin F, et al. Soluble Oligomers of PolyQ-Expanded Huntingtin Target a Multiplicity of Key Cellular Factors. *Mol Cell*. 2016;63(6):950-964.
48. Aiken CT, Steffan JS, Guerrero CM, et al. Phosphorylation of threonine 3: Implications for huntingtin aggregation and neurotoxicity. *J Biol Chem*. 2009;284(43):29427-29436.
49. Shahmoradian SH, Lewis AJ, Genoud C, et al. crowded organelles and lipid membranes. *Nat Neurosci*. 2019;22(July).
50. Mahul-Mellier A-L, Burtscher J, Maharjan N, et al. The process of Lewy body formation, rather than simply alpha-synuclein fibrillization, is the major driver of neurodegeneration. *Proc Natl Acad Sci*. 2020.
51. Valenza M, Rigamonti D, Goffredo D, et al. Dysfunction of the cholesterol biosynthetic pathway in Huntington's disease. *J Neurosci*. 2005;25(43):9932-9939.
52. Del Toro D, Xifró X, Pol A, et al. Altered cholesterol homeostasis contributes to enhanced excitotoxicity in Huntington's disease. *J Neurochem*. 2010;115(1):153-167.
53. Culver BP, DeClercq J, Dolgalev I, et al. Huntington's Disease Protein Huntingtin Associates with its own mRNA. *J Huntingtons Dis*. 2016;5(1):39-51.
54. Bowles KR, Stone T, Holmans P, Allen ND, Dunnett SB, Jones L. SMAD transcription factors are altered in cell models of HD and regulate HTT expression. *Cell Signal*. 2017;31:1-14.
55. Feyeux M, Bourgois-Rocha F, Redfern A, et al. Early transcriptional changes linked to naturally occurring Huntington's disease mutations in neural derivatives of human embryonic stem cells. *Hum Mol Genet*. 2012;21(17):3883-3895.
56. Borovecki F, Lovrecic L, Zhou J, et al. Genome-wide expression profiling of human blood reveals biomarkers for Huntington's disease. *Proc Natl Acad Sci U S A*. 2005;102(31):11023-11028.
57. Runne H, Kuhn A, Wild EJ, et al. Analysis of potential transcriptomic biomarkers for Huntington's disease in peripheral blood. *Proc Natl Acad Sci U S A*. 2007;104(36):14424-14429.
58. Mastrokolias A, Ariyurek Y, Goeman JJ, et al. Huntington's disease biomarker progression profile identified by transcriptome sequencing in peripheral blood. *Eur J Hum Genet*. 2015;23(10):1349-1356.
59. Snapp EL, Hegde RS, Francolini M, et al. Formation of stacked ER cisternae by low

affinity protein interactions. *J Cell Biol*. 2003;163(2):257-269.
60. McCaughey J, Miller VJ, Stevenson NL, et al. TFG Promotes Organization of Transitional ER and Efficient Collagen Secretion. *Cell Rep*. 2016;15(8):1648-1659.
61. Witte K, Schuh AL, Hegermann J, et al. TFG-1 function in protein secretion and oncogenesis. *Nat Cell Biol*. 2011;13(5):550-558.
62. Ray PD, Huang B-W, Tsuji Y. Reactive oxygen species (ROS) homeostasis and redox regulation in cellular signaling. *Cell Signal*. 2012;24(5):981-990.
63. Chang DTW, Rintoul GL, Pandipati S, Reynolds IJ. Mutant huntingtin aggregates impair mitochondrial movement and trafficking in cortical neurons. *Neurobiol Dis*. 2006;22(2):388-400.
64. Kim M, Lee H, Laforet G, et al. Mutant Huntingtin Expression in Clonal Striatal Cells : Dissociation of Inclusion Formation and Neuronal Survival by Caspase Inhibition. *J Neurosci*. 1999;19(3):964-973.
65. Luo H, Cao L, Liang X, Du A, Peng T, Li H. Herp Promotes Degradation of Mutant Huntingtin: Involvement of the Proteasome and Molecular Chaperones. *Mol Neurobiol*. 2018.
66. Saudou F, Finkbeiner S, Devys D, Greenberg ME. Huntingtin acts in the nucleus to induce apoptosis but death does not correlate with the formation of intranuclear inclusions. *Cell*. 1998;95(1):55-56.
67. Lunkes A, Mandel JL. A cellular model that recapitulates major pathogenic steps of Huntington's disease. *Hum Mol Genet*. 1998;7(9):1355-1361.
68. Hackam AS, Singaraja R, Wellington CL, et al. The influence of huntingtin protein size on nuclear localization and cellular toxicity. *J Cell Biol*. 1998;141(5):1097-1105.
69. Cooper JK, Schilling G, Peters MF, et al. Truncated N-terminal fragments of huntingtin with expanded glutamine repeats form nuclear and cytoplasmic aggregates in cell culture. *Hum Mol Genet*. 1998;7(5):783-790.
70. Labbadia J, Morimoto RI. Huntington's disease: Underlying molecular mechanisms and emerging concepts. *Trends Biochem Sci*. 2013;38(8):378-385.
71. Ellrichmann G, Reick C, Saft C, Linker RA. The role of the immune system in Huntington's disease. *Clin Dev Immunol*. 2013;2013.
72. Forno LS, Norville RL. Ultrastructure of Lewy bodies in the stellate ganglion. *Acta Neuropathol*. 1976;34(3):183-197.
73. Gai WP, Yuan HX, Li XQ, Power JTH, Blumbergs PC, Jensen PH. In situ and in vitro study of colocalization and segregation of α-synuclein, ubiquitin, and lipids in Lewy bodies. *Exp Neurol*. 2000;166(2):324-333.
74. DiFiglia M. Aggregation of Huntingtin in Neuronal Intranuclear Inclusions and Dystrophic Neurites in Brain. *Science (80-)*. 1997;277(5334):1990-1993.
75. Tellez-Nagel I, Johnson AB, Terry RD. Studies on brain biopsies of patients with Huntington's chorea. *J Neuropathol Exp Neurol*. 1974;33(2):308-332.
76. Choo YS, Johnson GVW, MacDonald M, Detloff PJ, Lesort M. Mutant huntingtin directly increases susceptibility of mitochondria to the calcium-induced permeability transition and cytochrome c release. *Hum Mol Genet*. 2004;13(14):1407-1420.
77. Song W, Chen J, Petrilli A, et al. Mutant huntingtin binds the mitochondrial fission GTPase dynamin-related protein-1 and increases its enzymatic activity. *Nat Med*. 2011;17(3):377-383.
78. Brennan WA, Bird ED, Aprille JR. Regional Mitochondrial Respiratory Activity in Huntington's Disease Brain. *J Neurochem*. 1985;44(6):1948-1950.
79. Gu M, Gash MT, Mann VM, Javoy-Agid F, Cooper JM, Schapira AHV. Mitochondrial defect in Huntington's disease caudate nucleus. *Ann Neurol*. 1996;39(3):385-389.
80. Browne SE, Bowling AC, MacGarvey U, et al. Oxidative damage and metabolic dysfunction in huntington's disease: Selective vulnerability of the basal ganglia. *Ann Neurol*. 1997;41(5):646-653.
81. Stephens DJ. De novo formation, fusion and fission of mammalian COPII-coated endoplasmic reticulum exit sites. *EMBO Rep*. 2003;4(2):210-217.
82. Farhan H, Weiss M, Tani K, Kaufman RJ, Hauri HP. Adaptation of endoplasmic

reticulum exit sites to acute and chronic increases in cargo load. *EMBO J*. 2008;27(15):2043-2054.
83. Vidal R, Caballero B, Couve a, Hetz C. Converging pathways in the occurrence of endoplasmic reticulum (ER) stress in Huntington's disease. *Curr Mol Med*. 2011;11:1-12.
84. Jiang R, Diaz-Castro B, Looger LL, Khakh BS. Dysfunctional Calcium and Glutamate Signaling in Striatal Astrocytes from Huntington's Disease Model Mice. *J Neurosci*. 2016;36(12):3453-3470.
85. Lee K, Huh S, Lee S, Wu Z, Kim A, Kang H. Altered ER – mitochondria contact impacts mitochondria calcium homeostasis and contributes to neurodegeneration in vivo in disease models. *Proc Natl Acad Sci*. 2018;115(42).
86. El-Daher M-T, Hangen E, Bruyere J, et al. Huntingtin proteolysis releases non-polyQ fragments that cause toxicity through dynamin 1 dysregulation. *EMBO J*. 2015;34(17):2255-2271.
87. Leitman J, Ulrich Hartl F, Lederkremer GZ. Soluble forms of polyQ-expanded huntingtin rather than large aggregates cause endoplasmic reticulum stress. *Nat Commun*. 2013;4:1-10.
88. Higo T, Hamada K, Hisatsune C, et al. Mechanism of ER Stress-Induced Brain Damage by IP3 Receptor. *Neuron*. 2010;68(5):865-878.
89. Legleiter J, Mitchell E, Lotz GP, et al. Mutant huntingtin fragments form oligomers in a polyglutamine length-dependent manner in Vitro and in Vivo. *J Biol Chem*. 2010;285(19):14777-14790.
90. Iaz-Hernandezı M, Moreno-herrero F, Gomez-Ramos P, et al. Biochemical , Ultrastructural , and Reversibility Studies on Huntingtin Filaments Isolated from Mouse and Human Brain. *J Neurosci*. 2004;24(42):9361-9371.
91. Poirier MA, Li H, Macosko J, Cai S, Amzel M, Ross CA. Huntingtin spheroids and protofibrils as precursors in polyglutamine fibrilization. *J Biol Chem*. 2002;277(43):41032-41037.
92. Peters MF, Nucifora FC, Kushi J, et al. Nuclear targeting of mutant huntingtin increases toxicity. *Mol Cell Neurosci*. 1999;14(2):121-128.
93. Benn CL, Landles C, Li H, et al. Contribution of nuclear and extranuclear polyQ to neurological phenotypes in mouse models of Huntington's disease. *Hum Mol Genet*. 2005;14(20):3065-3078.
94. Greiner ER, Yang XW. Huntington's disease: Flipping a switch on huntingtin. *Nat Chem Biol*. 2011;7(7):412-414.
95. Deguire SM, Ruggeri FS, Fares M, et al. N-terminal Huntingtin (Htt) phosphorylation is a molecular switch regulating Htt aggregation, helical conformation, internalization, and nuclear targeting. *J Biol Chem*. 2018;(12).
96. Michalek M, Salnikov ES, Werten S, Bechinger B. Membrane interactions of the amphipathic amino terminus of huntingtin. *Biochemistry*. 2013;52(5):847-858.
97. Burke KA, Kauffman KJ, Umbaugh CS, Frey SL, Legleiter J. The interaction of polyglutamine peptides with lipid membranes is regulated by flanking sequences associated with huntingtin. *J Biol Chem*. 2013;288(21):14993-15005.
98. Chaibva M, Gao X, Jain P, Campbell WA, Frey SL, Legleiter J. Sphingomyelin and GM1 Influence Huntingtin Binding to, Disruption of, and Aggregation on Lipid Membranes. *ACS Omega*. 2017;3(1):273-285. doi:10.1021/acsomega.7b01472
99. Isas JM, Langen R, Siemer AB. Solid-State Nuclear Magnetic Resonance on the Static and Dynamic Domains of Huntingtin Exon-1 Fibrils. *Biochemistry*. 2015;54(25):3942-3949.
100. Lin H, Boatz JC, Krabbendam IE, et al. Fibril polymorphism affects immobilized non-amyloid flanking domains of huntingtin exon1 rather than its polyglutamine core. *Nat Commun*. 2017;8(May):1-12.
101. Bugg CW, Isas JM, Fischer T, Patterson PH, Langen R. Structural features and domain organization of huntingtin fibrils. *J Biol Chem*. 2012;287(38):31739-31746.
102. Boatz JC, Piretra T, Lasorsa A, Matlahov I, Conway JF, Patrick C. A. van der Wel.

Protofilament structure and supramolecular polymorphism of aggregated mutant huntingtin exon 1. *J Mol Biol*. 2020.
103. Gao YG, Yan XZ, Song AX, et al. Structural Insights into the Specific Binding of Huntingtin Proline-Rich Region with the SH3 and WW Domains. *Structure*. 2006;14(12):1755-1765.
104. Li L, Liu H, Dong P, et al. Real-time imaging of Huntingtin aggregates diverting target search and gene transcription. *Elife*. 2016;5(AUGUST):1-29.
105. Aktar F, Burudpakdee C, Polanco M, et al. The huntingtin inclusion is a dynamic phase-separated compartment. *Life Sci Alliance*. 2019;2(5):1-14.
106. Posey AE, Ruff KM, Harmon TS, et al. Profilin reduces aggregation and phase separation of huntingtin N-terminal fragments by preferentially binding to soluble monomers and oligomers. *J Biol Chem*. 2018;293(10):3734-3746.
107. Hazeki N, Tsukamoto T, Yazawa I, et al. Ultrastructure of nuclear aggregates formed by expressing an expanded polyglutamine. *Biochem Biophys Res Commun*. 2002;294(2):429-440.
108. Schipper-Krom S, Juenemann K, Jansen AH, et al. Dynamic recruitment of active proteasomes into polyglutamine initiated inclusion bodies. *FEBS Lett*. 2014;588(1):151-159.
109. Juenemann K, Jansen AHP, van Riel L, et al. Dynamic recruitment of ubiquitin to mutant huntingtin inclusion bodies. *Sci Rep*. 2018;8(1):1405.
110. Hipp MS, Patel CN, Bersuker K, et al. Indirect inhibition of 26S proteasome activity in a cellular model of Huntington's disease. *J Cell Biol*. 2012;196(5):573-587.
111. Bennett EJ, Shaler TA, Woodman B, et al. Global changes to the ubiquitin system in Huntington's disease. *Nature*. 2007;448(7154):704-708.
112. Schipper-Krom S, Juenemann K, Reits EAJ. The ubiquitin-proteasome system in huntington's disease: Are proteasomes impaired, initiators of disease, or coming to the rescue? *Biochem Res Int*. 2012;2012.
113. Bansal M, Moharir SC, Swarup G. Autophagy receptor optineurin promotes autophagosome formation by potentiating LC3-II production and phagophore maturation. *Commun Integr Biol*. 2018;11(2):1-4.
114. N'Diaye EN, Debnath J, Brown EJ. Ubiquilins accelerate autophagosome maturation and promote cell survival during nutrient starvation. *Autophagy*. 2009;5(4):573-575.
115. Baker B, Geng S, Chen K, et al. Alteration of lysosome fusion and low-grade inflammation mediated by super-low-dose endotoxin. *J Biol Chem*. 2015;290(10):6670-6678.
116. Lu K, Psakhye I, Jentsch S. Autophagic clearance of PolyQ proteins mediated by ubiquitin-Atg8 adaptors of the conserved CUET protein family. *Cell*. 2014;158(3):549-563.
117. Oguro A, Kubota H, Shimizu M, Ishiura S, Atomi Y. Protective role of the ubiquitin binding protein Tollip against the toxicity of polyglutamine-expansion proteins. *Neurosci Lett*. 2011;503(3):234-239.
118. Shimizu M, Oguro-Ando A, Ohoto-Fujita E, Atomi Y. *Toll-Interacting Protein Pathway: Degradation of an Ubiquitin-Binding Protein*. Vol 534. 1st ed. Elsevier Inc.; 2014.
119. Shen WC, Li HY, Chen GC, Chern Y, Tu PH. Mutations in the ubiquitin-binding domain of OPTN/optineurin interfere with autophagy- mediated degradation of misfolded proteins by a dominant-negative mechanism. *Autophagy*. 2015;11(4):685-700.
120. Korac J, Schaeffer V, Kovacevic I, et al. Ubiquitin-independent function of optineurin in autophagic clearance of protein aggregates. *J Cell Sci*. 2013;126(2):580-592.
121. Schwab C, Yu S, McGeer EG, McGeer PL. Optineurin in Huntington's disease intranuclear inclusions. *Neurosci Lett*. 2012;506(1):149-154.
122. Maruyama H, Kawakami H. Optineurin and amyotrophic lateral sclerosis. *Geriatr Gerontol Int*. 2013;13(3):528-532.
123. Deng Z, Purtell K, Lachance V, Wold MS, Chen S, Yue Z. Autophagy Receptors and Neurodegenerative Diseases. *Trends Cell Biol*. 2017;27(7):491-504.

124. Suhr ST, Senut MC, Whitelegge JP, Faull KF, Cuizon DB, Gage FH. Identities of sequestered proteins in aggregates from cells with induced polyglutamine expression. *J Cell Biol*. 2001;153(2):283-294.
125. Kim YE, Hosp F, Frottin F, et al. Soluble Oligomers of PolyQ-Expanded Huntingtin Target a Multiplicity of Key Cellular Factors. *Mol Cell*. 2016;63(6):950-964. doi:10.1016/j.molcel.2016.07.022
126. Kazantsev A, Preisinger E, Dranovsky A, Goldgaber D, Housman D. Insoluble detergent-resistant aggregates form between pathological and nonpathological lengths of polyglutamine in mammalian cells. *Proc Natl Acad Sci U S A*. 1999;96(20):11404-11409.
127. Scior A, Buntru A, Arnsburg K, et al. Complete suppression of Htt fibrilization and disaggregation of Htt fibrils by a trimeric chaperone complex. *EMBO J*. 2018;37(2):282-299.
128. Hjerpe R, Bett JS, Keuss MJ, et al. UBQLN2 Mediates Autophagy-Independent Protein Aggregate Clearance by the Proteasome. *Cell*. 2016;166(4):935-949.
129. Croce KR, Yamamoto A. A role for autophagy in Huntington's disease. *Neurobiol Dis*. 2019;122(August 2018):16-22.
130. Arrasate M, Mitra S, Schweitzer ES, Segal MR, Finkbeiner S. Inclusion body formation reduces levels of mutant huntingtin and the risk of neuronal death. *Nature*. 2004;431(7010):805-810.
131. Lu M, Banetta L, Young LJ, et al. Live-cell super-resolution microscopy reveals a primary role for diffusion in polyglutamine-driven aggresome assembly. *JBC*. 2018.
132. Liu KY, Shyu YC, Barbaro BA, et al. Disruption of the nuclear membrane by perinuclear inclusions of mutant huntingtin causes cell-cycle re-entry and striatal cell death in mouse and cell models of Huntington's disease. *Hum Mol Genet*. 2015;24(6):1602-1616.
133. Firdaus WJJ, Wyttenbach A, Giuliano P, Kretz-Remy C, Currie RW, Arrigo AP. Huntingtin inclusion bodies are iron-dependent centers of oxidative events. *FEBS J*. 2006;273(23):5428-5441.
134. Miller J, Shaby BA, Mitra S, Masliah E, Finkbeiner S. Quantitative Relationships between Huntingtin Levels , Polyglutamine Length , Inclusion Body Formation , and Neuronal Death Provide Novel Insight into Huntington ' s Disease Molecular Pathogenesis. *J Neurosci*. 2010;30(31):10541-10550.
135. Cha JJ. Transcriptional dysregulation in Huntington ' s disease. *Trends Neurosci*. 2000:387-392.
136. Moumné L, Betuing S, Caboche J. Multiple Aspects of Gene Dysregulation in Huntington's Disease. *Front Neurol*. 2013;4(October):1-10.
137. Valor L, Viosca J, Lopez-Atalaya J, Barco A. Lysine Acetyltransferases CBP and p300 as Therapeutic Targets in Cognitive and Neurodegenerative Disorders. *Curr Pharm Des*. 2013;19(28):5051-5064.
138. Faber PW, Barnes GT, Srinidhi J, Chen J, Gusella JF, MacDonald ME. Huntingtin interacts with a family of WW domain proteins. *Hum Mol Genet*. 1998;7(9):1463-1474.
139. Gao YG, Yang H, Zhao J, Jiang YJ, Hu HY. Autoinhibitory structure of the WW domain of HYPB/SETD2 regulates its interaction with the proline-rich region of huntingtin. *Structure*. 2014;22(3):378-386.
140. Dunah AW, Jeong H, Griffin A, et al. Sp1 and TAFII130 transcriptional activity disrupted in early Huntington's disease. *Science (80-)*. 2002;296(5576):2238-2243.
141. Yamanaka T, Miyazaki H, Oyama F, et al. Mutant Huntingtin reduces HSP70 expression through the sequestration of NF-Y transcription factor. *EMBO J*. 2008;27(6):827-839.
142. Holbert S, Denghien I, Kiechle T, et al. The Gln-Ala repeat transcriptional activator CA150 interacts with huntingtin: Neuropathologic and genetic evidence for a role in Huntington's disease pathogenesis. *Proc Natl Acad Sci U S A*. 2001;98(4):1811-1816.
143. Van Roon-Mom WMC, Reid SJ, Jones AL, MacDonald ME, Faull RLM, Snell RG. Insoluble TATA-binding protein accumulation in Huntington's disease cortex. *Mol Brain*

Res. 2002;109(1-2):1-10.
144. Rusten TE, Filimonenko M, Rodahl LM, Stenmark H, Simonsen A. ESCRTing autophagic clearance of aggregating proteins. *Autophagy*. 2008;4(2):233-236.
145. Crotti A, Glass CK. The choreography of neuroinflammation in Huntington's disease. *Trends Immunol*. 2015;36(6):364-373.
146. Bossy-Wetzel E, Petrilli A, Knott AB. Mutant Huntintin and Mitochondrial Dysfunction. *Trends Neurosci*. 2008;31(12):609-616. doi:10.1016/j.tins.2008.09.004.MUTANT
147. A. Crotti, Benner C, Kerman B, et al. Mutant Huntingtin promotes autonomous microglia activation via myeloid lineage-determining factors. *Nat Neurosci*. 2014;17(4):513-521.
148. Jordan M, Schallhorn A, Wurm FM, Francisco SS. Transfecting mammalian cells : optimization of critical parameters affecting calcium-phosphate precipitate formation. *Nucleic Acids Res*. 1996;24(4):596-601.
149. Dorin-Semblat D, Demarta-Gatsi C, Hamelin R, et al. Malaria parasite-infected erythrocytes secrete PfCK1, the Plasmodium homologue of the pleiotropic protein kinase casein kinase 1. *PLoS One*. 2015;10(12):1-22.
150. Rappsilber J, Mann M, Ishihama Y. Protocol for micro-purification, enrichment, pre-fractionation and storage of peptides for proteomics using StageTips. *Nat Protoc*. 2007;2(8):1896-1906.
151. Cox J, Mann M. MaxQuant enables high peptide identification rates, individualized p.p.b.-range mass accuracies and proteome-wide protein quantification. *Nat Biotechnol*. 2008;26(12):1367-1372.
152. Cox J, Hein MY, Luber CA, Paron I, Nagaraj N, Mann M. Accurate proteome-wide label-free quantification by delayed normalization and maximal peptide ratio extraction, termed MaxLFQ. *Mol Cell Proteomics*. 2014;13(9):2513-2526.
153. Tyanova S, Temu T, Sinitcyn P, et al. The Perseus computational platform for comprehensive analysis of (prote)omics data. *Nat Methods*. 2016;13(9):731-740.
154. Hubner NC, Bird AW, Cox J, et al. Quantitative proteomics combined with BAC TransgeneOmics reveals in vivo protein interactions. *J Cell Biol*. 2010;189(4):739-754.
155. CoreTeam R. *R: A Language and Environment for Statistical Computing.* Vol 2.; 2019.
156. Makrecka-Kuka M, Krumschnabel G, Gnaiger E. High-resolution respirometry for simultaneous measurement of oxygen and hydrogen peroxide fluxes in permeabilized cells, tissue homogenate and isolated mitochondria. *Biomolecules*. 2015;5(3):1319-1338.
157. Pesta D, Gnaiger E. High-Resolution Respirometry: OXPHOS Protocols for Human Cells and Permeabilized Fibers from Small Biopsies of Human Muscle BT - Mitochondrial Bioenergetics: Methods and Protocols. In: Palmeira CM, Moreno AJ, eds. Totowa, NJ: Humana Press; 2012:25-58.
158. Burtscher J, Zangrandi L, Schwarzer C, Gnaiger E. Differences in mitochondrial function in homogenated samples from healthy and epileptic specific brain tissues revealed by high-resolution respirometry. *Mitochondrion*. 2015;25:104-112.

Author contributions

H.A.L conceived and supervised the study. H.A.L, N.R and A.L.M.M designed all the experiments and wrote the paper. N.R performed and analyzed the confocal imaging, the electron microscopy and the 3D imaging reconstruction, quantitative proteomic experiments and the biochemistry experiments. A.L.M.M performed and analyzed the CLEM experiment and analyzed the proteomic data. N.M designed and analyzed the proteomic data. J.B designed, performed, and analyzed the high resolution respirometry experiments. A.P helped to performed and analyze the confocal imaging experiments. M.C prepared the samples for CLEM and acquired the EM images. G.K supervised the EM-related experiments and 3D imaging reconstruction, and contributed to the interpretation of the data. V.R and H.F designed, performed, and analyzed the experiments related to ER. All authors reviewed and contributed to the writing.

Competing interests statement

Authors declare no competing financial interests in association with this manuscript.

Acknowledgments

This work was supported by funding from the Ecole Polytechnique Fédérale de Lausanne (EPFL) and the CHDI Foundation (H.A.L, N.R, A.L.M, N.M, J.B and A.P). We thank Dr. Arne Seitz and the staff at the Bio-imaging Core Facility (BioP, EPFL) for their technical support and valuable discussions. We are grateful to the Proteomics Core Facility (EPFL): Dr Diego Chiappe, Dr. Romain Hamelin and Dr. Florence Armand for their guidance, helpful discussions and support with the proteomic studies. We also thank Stéphanie Rosset and Anaëlle Dubois at the Bio-EM Core facility (EPFL) for their technical support. We are grateful to the research associates in the Lashuel Lab: Driss Boudeffa and Ricci Jonathan for their continuous technical assistance. We thank Andrea Caricasole (IRBM) for kindly providing the pCMV mammalian expression vector encoding for the basic Httex1 constructs. We would also like to thank Magda Zachara (EPFL) for the Bodipy staining and useful discussions. Figure 8 has been prepared using BioRender.

Figures

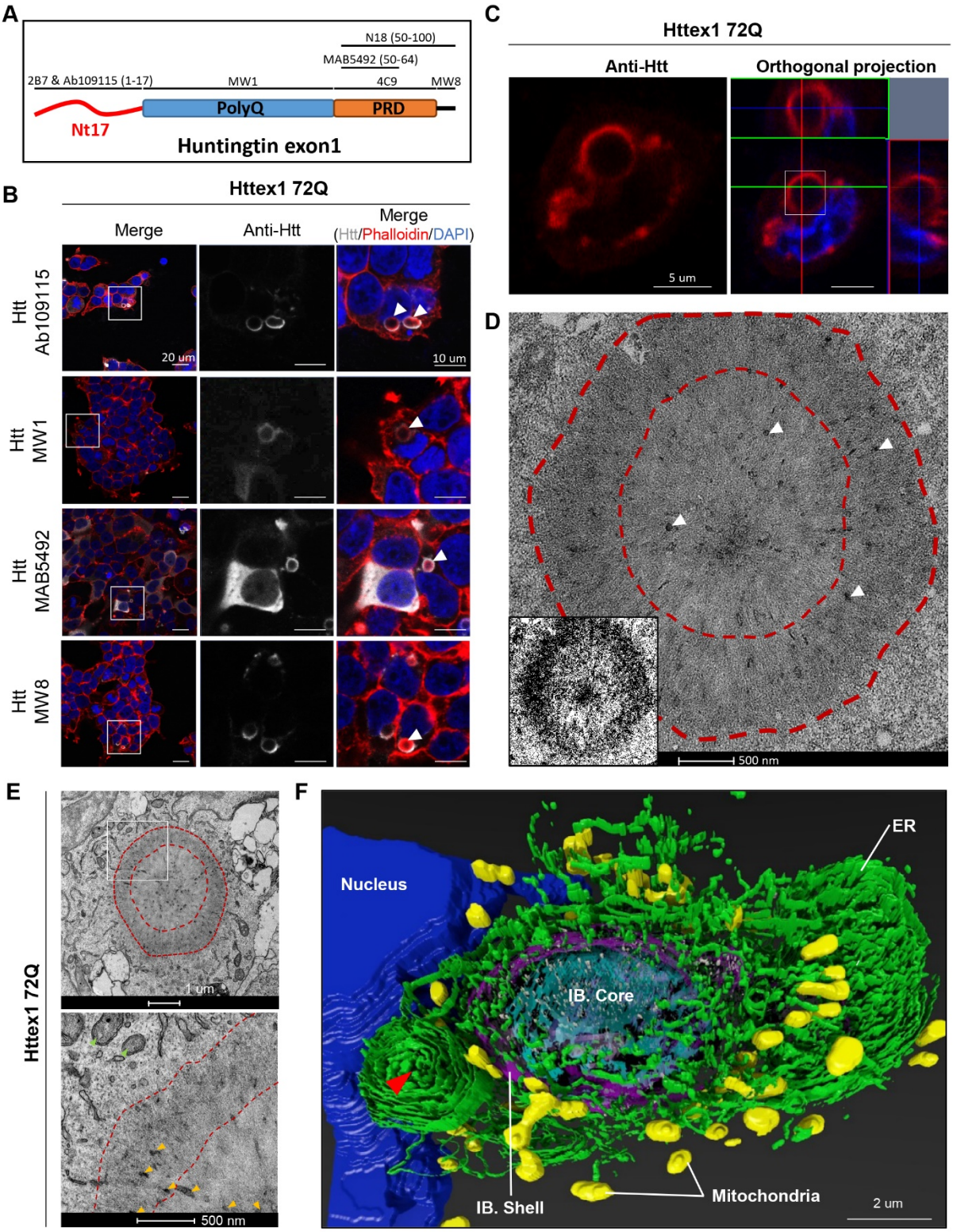

Figure 1. Confocal microscopy and CLEM revealed the ring-like structure of the Httex1 72Q inclusions formed in HEK cells. A. Epitope mapping of the Httex1 antibodies. **B.** Httex1 72Q inclusions that formed 48h after transfection in HEK cells were detected by ICC staining

combined with confocal imaging. All the htt antibodies showed strong immunoreactivity to the periphery of the Httex1 inclusions. The nucleus was counterstained with DAPI (blue) and the F-actin with phalloidin (red). White arrows indicate the colocalization of the F-actin with the ring-like structure of Httex1 inclusions. Scale bar = 20 µm (left-hand panels) and 10µm (middle and right-hand panels). **C. and D.** 48h post-transfection, HEK cells were fixed, and ICC against Httex1 was performed and imaged by confocal microscopy (**C**). Scale bars = 5 µm. The selected area of the cells (white square) was then examined by EM (**D**). Pieces of membranes and vesicles are indicated with the white arrowheads. Binary image (inset) was generated from the electron micrograph using a median filtering and Otsu intensity threshold, allowing for a better distinction between the core and the shell ultrastructure of the tag-free Httex1 inclusion. Scale bar = 500 nm. **E.** Representative electron micrograph of Httex1 72Q cellular inclusion and higher magnification (white square) shown in the lower panel. Dash lines delimit the aggregate and the core of the inclusion. Internalized membranous structures and the mitochondria are indicated, respectively, by the orange arrowheads and the green arrowheads. Scale bar = 1 µm (top panel) and 500nm (bottom panel) **F.** 3D model of Httex1 72Q cellular inclusion and surrounding organelles (top view). The Httex1 inclusion body (IB.) shell is represented in purple and the IB. core in cyan. ER membranes shown as green, intra-inclusion membranous structures are displayed in white, the nucleus is shown in blue, and the mitochondria are shown in yellow. A red arrow highlights the formation of stacked ER cisternae. Scale bar = 2 µm.

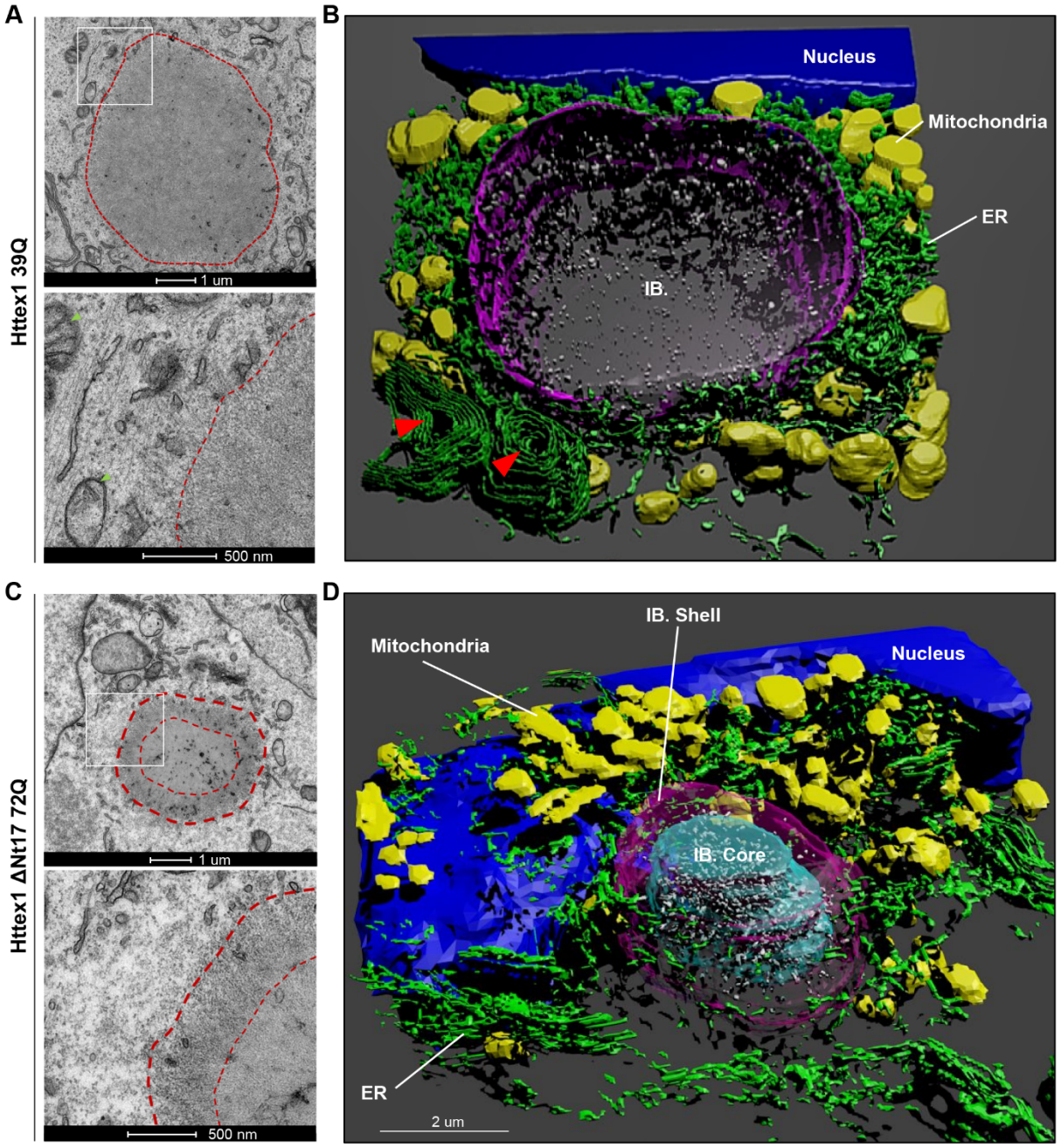

Figure 2. PolyQ expansion, but not the Nt17 domain, plays a critical role in shaping the structural architecture of the Httex1 inclusions. A. Representative electron micrograph of Httex1 39Q inclusion formed 48h after transfection in HEK. The white square indicates the area shown in the lower panel at higher magnification. Dash lines delimit the inclusion. Httex1 39Q inclusions appeared less dense than the Httex1 72Q inclusions. Scale bar = 1 µm (top panel) and 500 nm (bottom panel). **B.** 3D model of the Httex1 39Q inclusion body (IB.) is shown in purple, surrounded by mitochondria (yellow) and ER structures (green). A red arrow highlights the formation of stacked ER cisternae close to the Httex1 39Q inclusion. Intra-inclusion membranous structures are shown in white. The nucleus is highlighted in blue. Scale bar = 2 µm. **C.** Representative electron micrograph of Httex1 ΔNt17 72Q inclusion formed 48h

after transfection in HEK. The white square indicates the higher magnification shown in the lower panel. Dash lines delimit the inclusion and the core of the inclusion. Scale bar = 1 µm (top panel) and 500 nm (bottom panel). **D.** 3D model of the Httex1 ΔNt17 72Q inclusion. The Httex1 inclusion body (IB.) shell is represented in purple, the IB. core in cyan, the ER membranes in green, the intra-inclusion membranous structures in white, the nucleus in blue, and the mitochondria in yellow. Scale bar = 2 µm.

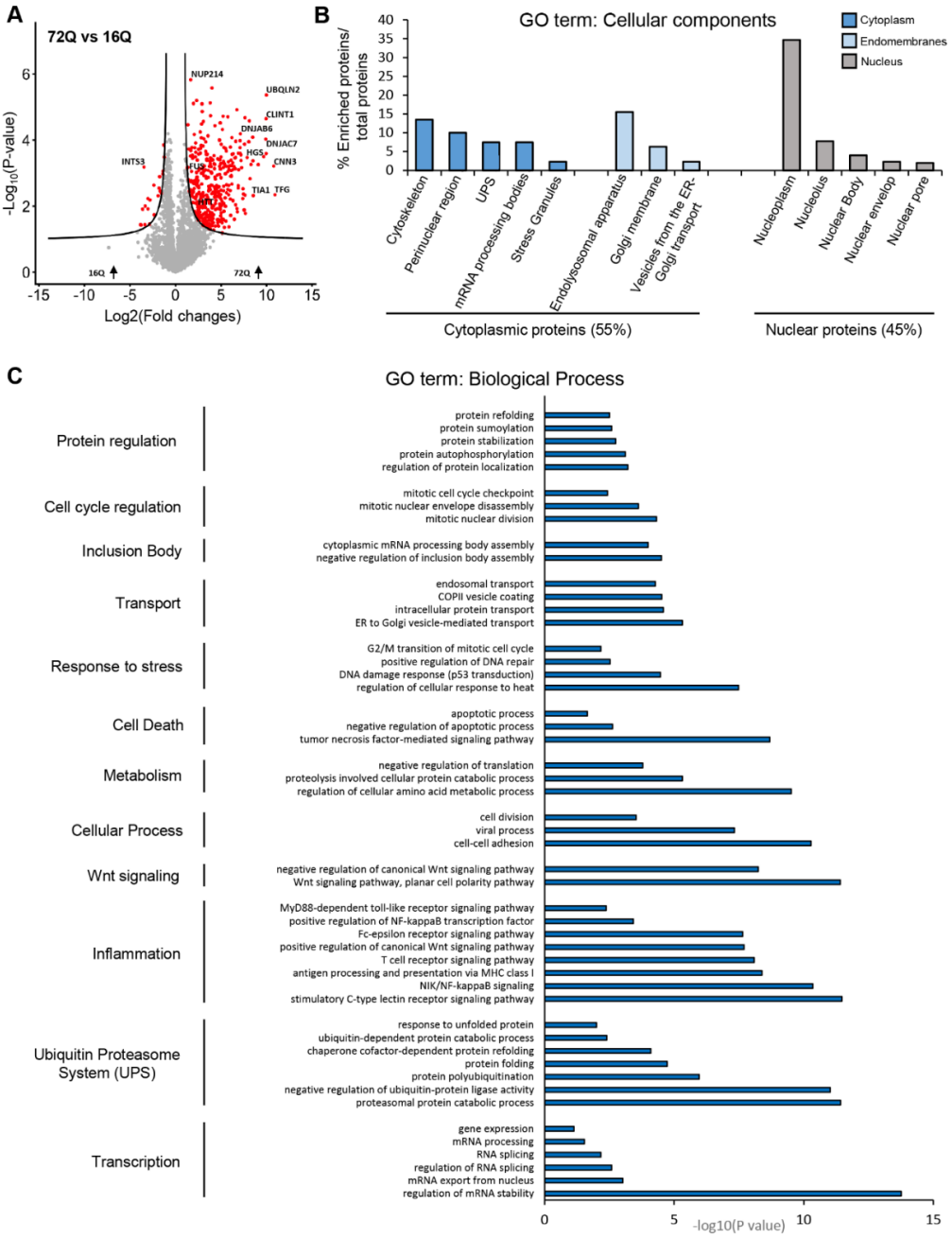

Figure 3. Proteomic analysis of the enriched protein contents found in the insoluble fraction of HEK expressing Httex1 72Q reveals protein aggregation and stress response pathways. Urea insoluble proteins from HEK expressing Httex1 72Q or Httex1 16Q of 3 independent experiments were extracted 48h after transfection and analyzed using LC-MS/MS. **A.** Identified proteins were plotted using a volcano plot. Black lines represent the false discovery rate (FDR) <0.05; the threshold of significance (S0) of 0.5 was assigned for the subsequent analysis. **B-C**. Proteins significantly enriched in Httex1 72Q (red dots in the right part of the volcano plot) were classified by cellular component (**B**) or biological processes (**C**) using Gene Ontology (GO) term and DAVID enrichment ($-\log_{10}$(p-value >1) analyses.

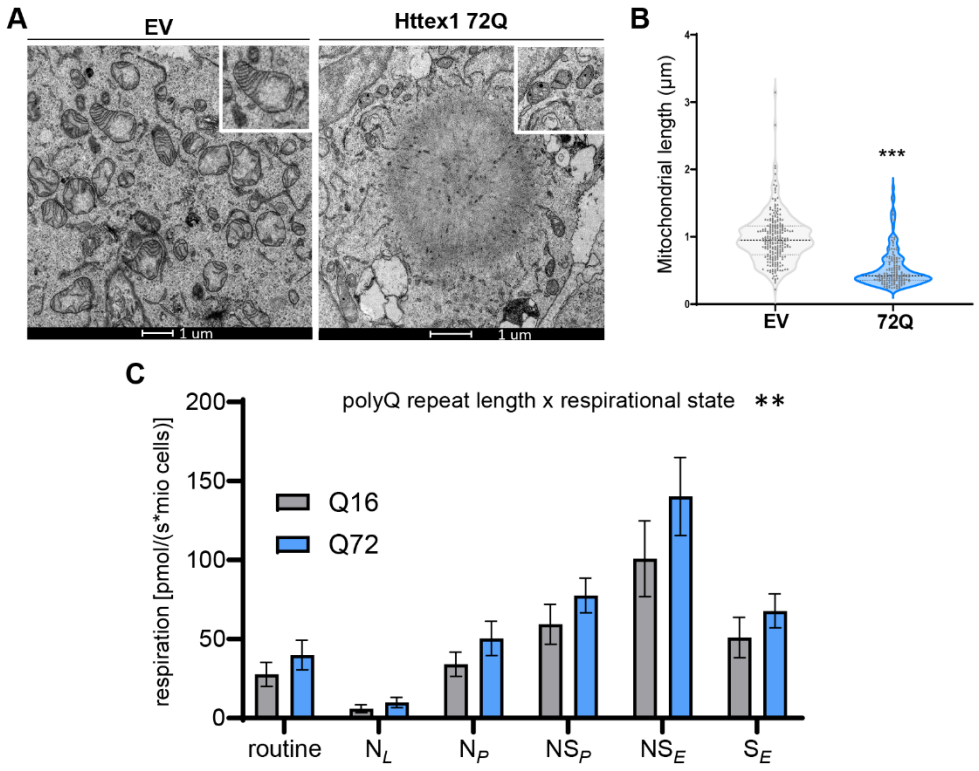

Figure 4. Formation of Httex1 72Q inclusions induces mitochondrial alterations. A. Electron micrographs of mitochondria in HEK cells overexpressing EV (Empty Vector) or Httex1 72Q. The insets depict higher magnification of the mitochondria found at the periphery of the Httex1 72Q inclusions or representative in EV controls. Scale bars = 1 µm. **B.** Measurement of the mitochondrial length reveals a significant reduction in the size of the mitochondrial profile located in the proximity of the inclusions. **C.** HEK cells from 4 independent experiments were gently detached for high-resolution respirometry (HRR) 48h after transfection with indicated constructs. HRR was performed in respiration media (MIR05). After the measurement of routine respiration, cells were chemically permeabilized by digitonin, and different respirational states were subsequently induced using a substrate-uncoupler-inhibitor titration (SUIT) protocol. Routine respiration, NADH-driven, or complex 1-linked respiration after the addition of ADP (OXPHOS state) (NP), NADH- and succinate driven, or complex 1 and 2-linked respiration in the OXPHOS state (NSP), and in the uncoupled electron transport system (ETS) capacity (NSE), as well as succinate driven, or complex 2-linked respiration in the ETS state (SE) were assessed. (B) Unpaired t-test was performed. (C-G) The graphs represent the mean ± SD of 4 independent experiments. (C) ANOVA followed by a Tukey honest significant difference [HSD] post hoc test was performed. *P < 0.05, **P < 0.005, ***P < 0.001.

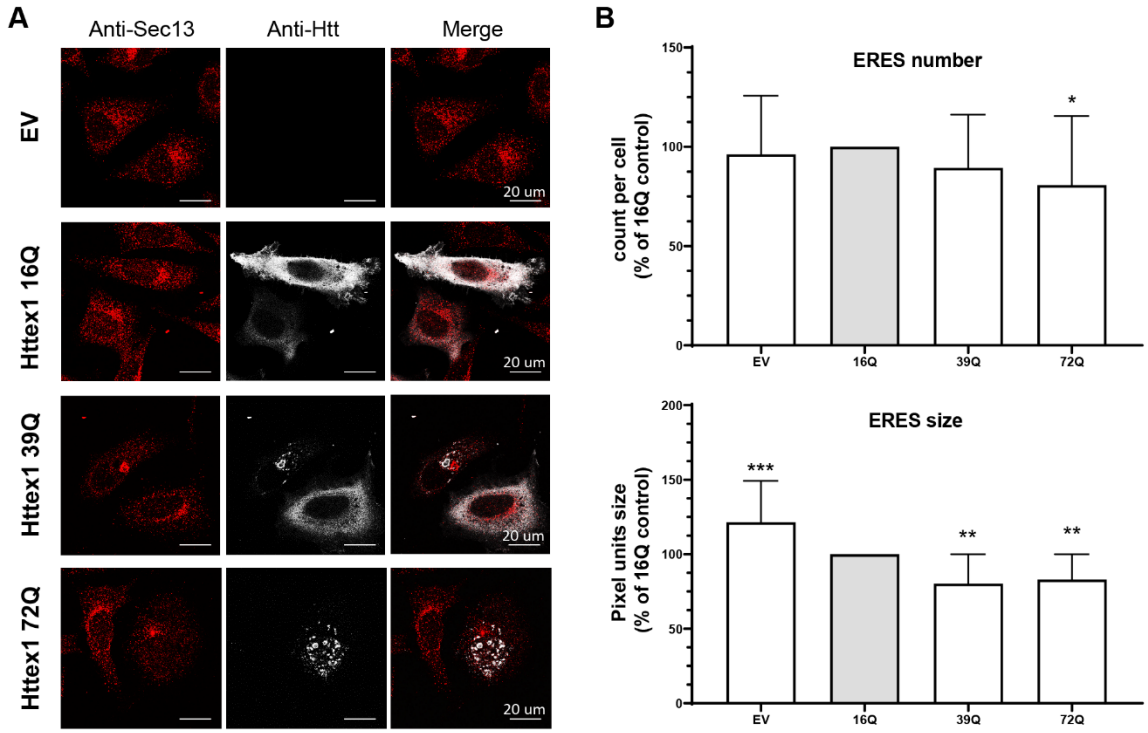

Figure 5. Httex1 inclusion formation induces the reduction of ER-exit sites. A. Representative confocal images of HeLa cells transfected with Httex1 16Q, 39Q, or 72Q or the Empty Vector (EV) as the negative control. Cells were fixed 48h after transfection and immunostained. Httex1 was detected with the MAB5492 Htt antibody (grey), and ER exit sites were detected with Sec13 (red). Scale bars = 20 µm. **B**. ERES number and size quantification from confocal imaging was performed using FIJI. The graphs represent the mean ± SD of 3 independent experiments represented as the relative percentage of the Httex1 16Q control. ANOVA followed by a Tukey honest significant difference [HSD] post hoc test was performed. *P < 0.05, **P < 0.005, ***P < 0.001.

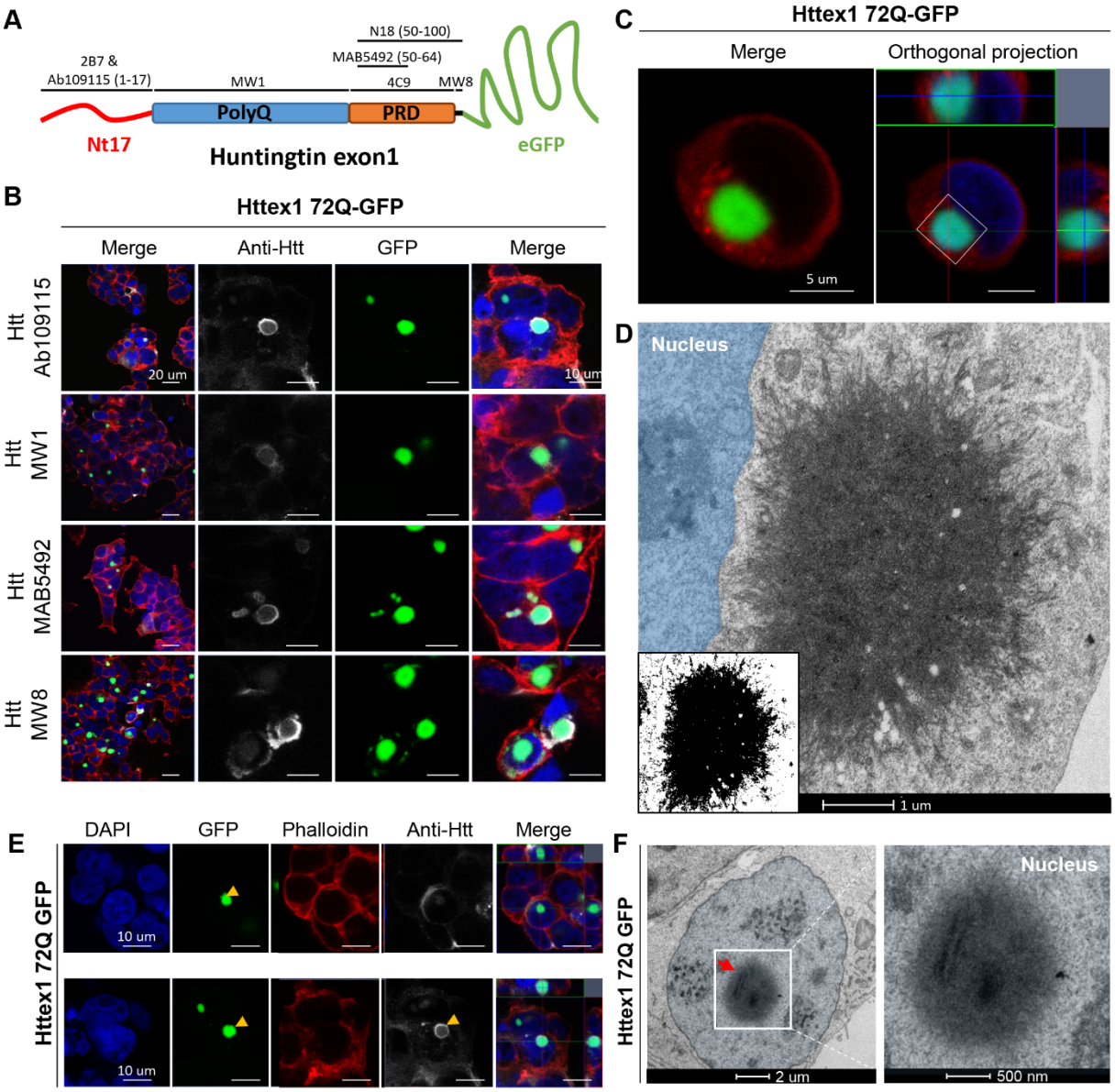

Figure 6. The addition of GFP to the C-terminal part of Httex1 induces a differential structural organization as revealed by ICC and CLEM. A. Epitope mapping of the Httex1 antibodies. **B.** Httex1 72Q-GFP inclusions formed 48h after transfection in HEK cells were detected by ICC staining combined with confocal imaging. All the htt antibodies showed strong immunoreactivity to the periphery of the Httex1 inclusions and slightly to the core. The nucleus was counterstained with DAPI (blue) and the F-actin with phalloidin (red). Scale bar = 20 µm (left-hand panels) and 10 µm (middle and right-hand panels). **C-D.** 48h post-transfection, HEK cells were fixed, and ICC against Httex1 was performed and imaged by confocal microscopy (**C**). Scale bars = 5 µm. The selected area of the cells (white square) was then examined by EM (**D**). A binary image (inset) was generated from the electron micrograph using a median filtering and Otsu intensity threshold, allowing for a better distinction of the inclusions'

morphology. Scale bar = 500 nm. **E.** Representative confocal images of Httex1 72Q-GFP nuclear inclusions formed in HEK cells 48h after transfection. Httex1 expression (grey) was detected using a specific antibody against the N-terminal part of Htt (amino acids 1-17; 2B7 or Ab109115) and GFP (green) directly visualized in the appropriate channel. The nucleus was counterstained with DAPI (blue), and phalloidin (red) was used to stain filamentous actin. Httex1 nuclear inclusions are indicated by yellow arrowheads. Scale bars = 10 µm. **F.** Electron micrograph of a representative Httex1 72Q-GFP inclusion. The white square indicates the area shown at higher magnification in the right-hand panel. The nucleus is highlighted in blue. Scale bar = 2 µm (left-hand panel) and 500 nm (right-hand panel).

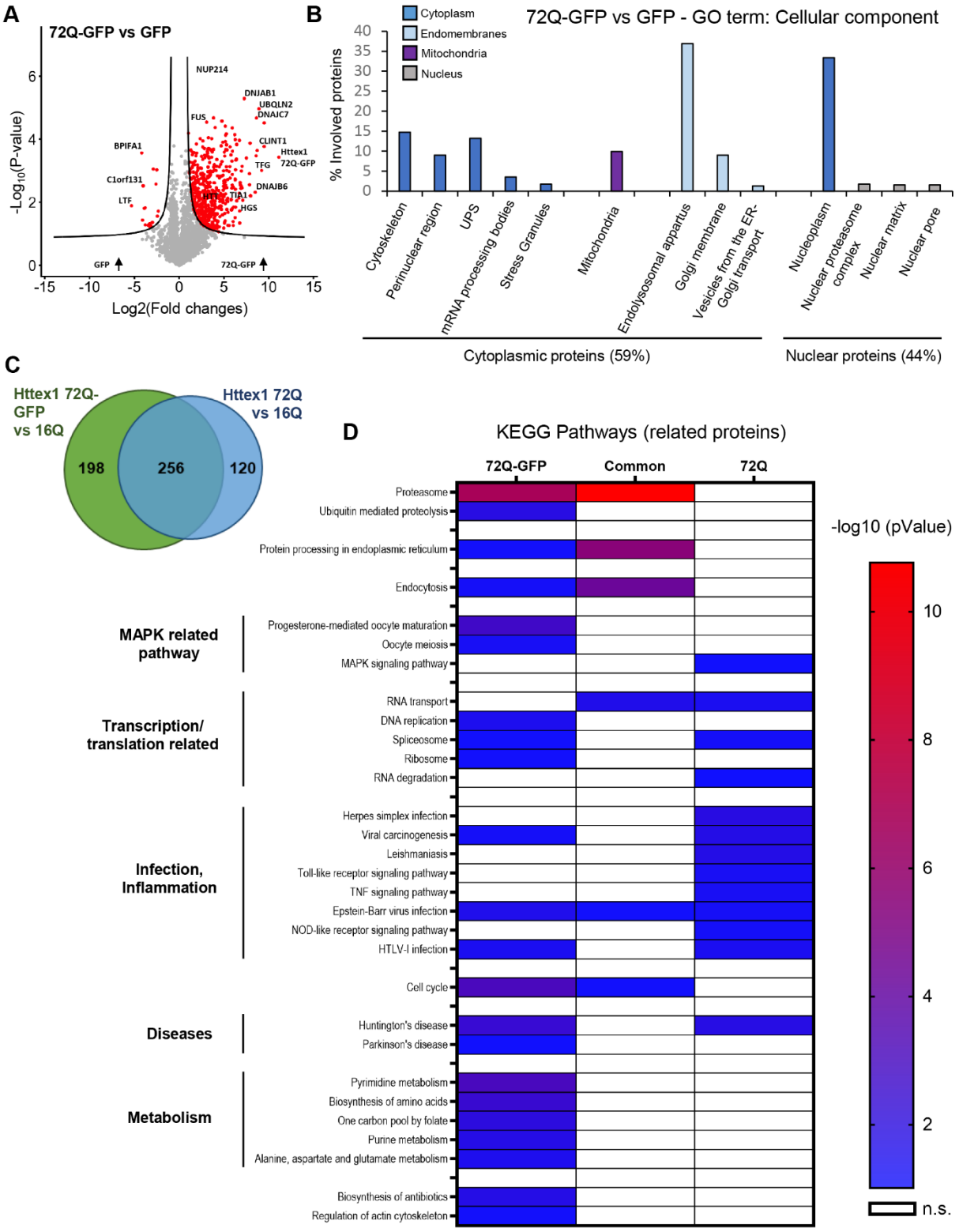

Figure 7. Proteomic analysis of Httex1 72Q-GFP in the Urea-insoluble fraction revealed 55% differences compared to tag-free Httex1 72Q for the proteins co-aggregated with Httex1. A. Identified proteins were plotted using volcano plot for the comparison of protein levels identified in the Urea-insoluble fraction 48h after Httex1 72Q-GFP or GFP transfection in HEK cells, in 3 independent experiments. Mean difference (Log2 (Fold-Change) on the X-

axis) between the Urea-insoluble fraction of HEK cells overexpressing Httex1 72Q-GFP or GFP were plotted against Log10 (p-Value) on the Y-axis (T-Test). False discovery rate (FDR) of 0.05 and a threshold of significance SO=0.5 were assigned for the subsequent analyses. **B.** Cell compartment classification of the proteins significantly enriched in the Urea-insoluble fraction of the HEK cells overexpressing Httex1 72Q-GFP versus those expressing GFP. Gene Ontology (GO) enrichment analyses were determined by DAVID analysis (p values<0.05). **C.** To compare the results obtained with Httex1 72Q GFP to tag-free Httex1 72Q, we represented the proteins enriched in Httex1 72Q vs Httex1 16Q compared to the proteins enriched in Httex1 72Q-GFP vs Httex1 16Q using a Venn diagram. In total, 256 proteins (44.6%) were found similar between the two conditions, 198 proteins (34.5%) were unique for Httex1 72-GFP enrichment, and 120 proteins (20.9%) were for Httex1 72Q enrichment. **D**. Kyoto Encyclopedia of Genes and Genomes (KEGG) Pathway Analysis of co-aggregated proteins with Httex1 72Q and Httex1 72Q-GFP. The heat map represents significative pathways (KEGG) enriched in the UREA-insoluble fractions extracted from the Venn diagram, Figure 7C: co-aggregated proteins unique to Httex1 72Q, unique to Httex1-72Q-GFP, and common to both conditions, all compared to Httex1 16Q control.

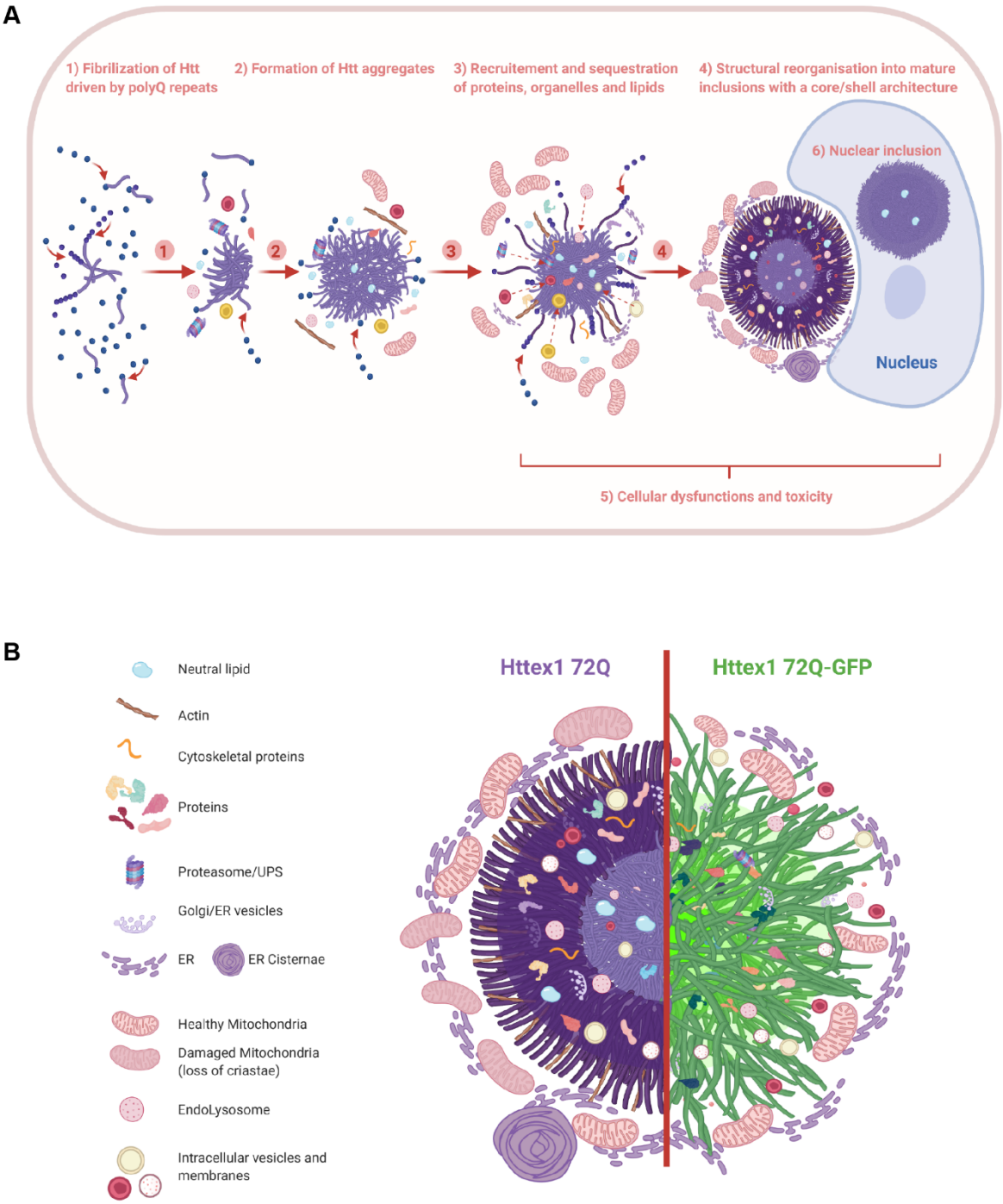

Figure 8. The formation of Huntingtin inclusions is driven primarily by the polyQ repeat domain and involves the active recruitment and sequestration of lipids, proteins, and membranous organelles. A. We separated the formation and organization of cytoplasmic Httex1 inclusions in different elements: 1) Even if the Nt17 can play a major role in early oligomerization steps, we showed that the fibrilization is driven by the polyQ repeats; 2) The initiation of inclusion formation was previously demonstrated to occur in a phase transition mechanism[17,131] and could first sequester proteins and organelles nearby either directly or indirectly; 3) During the growth of the inclusion, many cellular proteins, endomembranes, and

lipids are recruited and sequestered inside the cytoplasmic inclusions; 4) Mature cytoplasmic Httex1 inclusions formed in cells display a core and shell structural organization if the polyQ length is relatively long (72Q) but not close to the pathogenic threshold (39Q), even if inclusions are still formed in the second case. Cytoplasmic inclusion formation leads to the accumulation of mitochondria and ER network at the periphery; 5) Httex1 inclusion formation leads to the adaptation of the ER-mitochondrial network and respirational dysfunction, as well as significant toxicity after long-term incubation; 6) Nuclear inclusions do not display a distinct core/shell organization similar to the cytoplasmic inclusions, but they are still detected as a ring, as they are impervious to antibodies. Nuclear tag-free Httex1 inclusions are also enriched in neutral lipids. **B.** The depiction shows the distinct structural organization and cellular impact of Httex1 72Q (left) compared to Httex1 72Q-GFP (right). The arrangement and packing of Httex1 fibrils are different depending on the presence of GFP as well as the interactions, recruitment, and perturbation with surrounding organelles.